

# Liquid water transport in fuel cell gas diffusion layers

by

Aimy Ming Jii Bazylak

Bachelor of Science in Engineering, University of Saskatchewan, 2003

Master of Applied Science, University of Victoria, 2005

A Thesis Submitted in Partial Fulfillment of the  
Requirements for the Degree of

DOCTOR OF PHILOSOPHY

in the  
Department of Mechanical Engineering.

© AIMY MING JII BAZYLAK, 2008

University of Victoria

All rights reserved. This thesis may not be reproduced in whole or in part, by photocopy or other means, without the permission of the author.

# Liquid water transport in fuel cell gas diffusion layers

by

Aimy Ming Jii Bazylak

Bachelor of Science in Engineering, University of Saskatchewan, 2003

Master of Applied Science, University of Victoria, 2005

## Supervisory Committee

Dr. Ned Djilali, Supervisor  
(Dept. of Mechanical Engineering, University of Victoria)

Dr. David Sinton, Supervisor  
(Dept. of Mechanical Engineering, University of Victoria)

Dr. Zhong-Sheng (Simon) Liu, Supervisor  
(Dept. of Mechanical Engineering, University of Victoria)

Dr. Chris Papadopoulos, Outside Member  
(Dept. of Electrical & Computer Engineering, University of Victoria)

Dr. Matthew Mench, External Examiner  
(Dept. of Mechanical & Nuclear Engineering, Pennsylvania State University)

## Supervisory Committee

Dr. Ned Djilali, Supervisor  
(Dept. of Mechanical Engineering, University of Victoria)

Dr. David Sinton, Supervisor  
(Dept. of Mechanical Engineering, University of Victoria)

Dr. Zhong-Sheng (Simon) Liu, Supervisor  
(Dept. of Mechanical Engineering, University of Victoria)

Dr. Chris Papadopoulos, Outside Member  
(Dept. of Electrical & Computer Engineering, University of Victoria)

Dr. Matthew Mench, External Examiner  
(Dept. of Mechanical & Nuclear Engineering, Pennsylvania State University)

## Abstract

Liquid water management has a major impact on the performance and durability of the polymer electrolyte membrane fuel cell (PEMFC). The gas diffusion layer (GDL) of a PEMFC provides pathways for mass, heat, and electronic transport to and from the catalyst layers and bipolar plates. When the GDL becomes flooded with liquid water, the PEMFC undergoes mass transport losses that can lead to decreased performance and durability. The work presented in this thesis includes contributions that provide insight into liquid water transport behaviour in and on the surface of the GDL, as well as insight into how future GDLs could be designed to enhance water management.

The effects of compression on liquid water transport in the GDL and on the microstructure of the GDL are presented. It was found that compressed regions of the GDL provided preferential locations for water breakthrough, while scanning

electron microscopy (SEM) imaging revealed irreversible damage to the GDL due to compression at typical fuel cell assembly pressures.

The dynamic behaviour of droplet emergence and detachment in a simulated gas flow channel are also presented. It was found that on an initially dry and hydrophobic GDL, small droplets emerged and detached quickly from the GDL surface. However, over time, this water transport regime transitioned into that of slug formation and channel flooding. It was observed that after being exposed to a saturated environment, the GDL surface became increasingly prone to droplet pinning, which ultimately hindered droplet detachment and encouraged slug formation.

A pore network model featuring invasion percolation with trapping was employed to evaluate the breakthrough pattern predictions of designed porous media. These designed pore networks consisted of randomized porous media with applied diagonal and radial gradients. Experimental microfluidic pore networks provided validation for the designed networks. Diagonal biasing provided a means of directing water transport in the pore network, while radially biased networks provided the additional feature of reducing the overall network saturation. Since directed water transport and reduced saturation are both beneficial for the PEMFC GDL, it was proposed that biasing of this nature could be applied to improved GDL designs. Lastly, recommendations for future extensions of this research are proposed at the end of this thesis.

# Table of Contents

<b>Supervisory Committee</b>	<b>ii</b>
<b>Abstract</b>	<b>iii</b>
<b>Table of Contents</b>	<b>v</b>
<b>List of Tables</b>	<b>vii</b>
<b>List of Figures</b>	<b>viii</b>
<b>Acknowledgements</b>	<b>xiii</b>
<b>1 Introduction</b>	<b>1</b>
1.1 Background & Motivation . . . . .	1
1.2 Contributions . . . . .	3
1.3 Organization of the Thesis . . . . .	5
<b>2 Literature Review</b>	<b>8</b>
2.1 Liquid Water Visualization . . . . .	9
2.1.1 Nuclear Magnetic Resonance (NMR) . . . . .	9
2.1.2 Beam Interrogation . . . . .	11
2.1.3 Optical Photography . . . . .	15
2.1.4 Hypothesis . . . . .	17
2.2 Compression Effects . . . . .	17
2.3 Pore Network Modelling . . . . .	20
2.3.1 Background . . . . .	20
2.3.2 Application of Pore Network Modelling to the GDL . . . . .	23
<b>3 GDL Compression Effects</b>	<b>26</b>
3.1 Experimental . . . . .	26
3.1.1 Gas Diffusion Layer . . . . .	27
3.1.2 Apparatus . . . . .	27
3.1.3 Data Acquisition . . . . .	28

3.1.4	Results & Discussion . . . . .	29
3.2	Concluding Remarks . . . . .	35
<b>4</b>	<b>Dynamic Liquid Water Transport</b>	<b>45</b>
4.1	Apparatus . . . . .	45
4.2	Results & Discussion . . . . .	47
4.2.1	Droplet Growth . . . . .	47
4.2.2	Droplet Pinning . . . . .	48
4.2.3	Dynamic Breakthrough Locations . . . . .	50
4.2.4	Volume of Fluid Simulations . . . . .	51
4.3	Concluding Remarks . . . . .	52
<b>5</b>	<b>Pore Network Designs for Directed Transport</b>	<b>59</b>
5.1	Methodology . . . . .	60
5.1.1	Pore Network Modelling . . . . .	60
5.1.2	Microfluidic Pore Networks . . . . .	61
5.2	Pore Network Design . . . . .	62
5.2.1	Pore Network Structure . . . . .	62
5.2.2	Randomization . . . . .	62
5.3	Results & Discussion . . . . .	65
5.4	Concluding Remarks . . . . .	66
<b>6</b>	<b>Conclusions</b>	<b>75</b>
6.1	Future Work . . . . .	77
	<b>References</b>	<b>80</b>

# List of Tables

2.1	PEMFC visualization methods: summary of resolution capabilities. . .	25
3.1	Liquid Breakthrough Pressures . . . . .	36

# List of Figures

1.1	Schematic of a PEMFC. Hydrogen and oxygen diffuse through the GDLs and react at the catalyst layers. Protons released from the anode reaction travel through the ion conducting membrane, and electrons released travel through an external load. The electrochemical reactions at the anode and cathode drive the operation of the fuel cell by producing an electric potential and a current through an applied load. A Toray TGP-H-060 GDL is shown inset, outlined by a dashed red line. . . . .	7
3.1	Schematic of the fluorescence microscopy and GDL clamping apparatus.	37
3.2	Digital images from fluorescence microscopy showing the evolution of water transport at (a) $t = 4.9$ s, (b) $t = 5.2$ s, and (c) $t = 6.5$ s. Images to the left have been inverted for clarity, with the areas compressed by the O-ring shown as the area between the concentric dashed circles. To the right of each image is the three-dimensional rendering of the signal intensity. . . . .	38
3.3	Inverted fluorescence image at 5.2 s showing flow paths 1 and 2 shown in Fig. (3.4). The areas of the GDL that are compressed exist between the concentric dashed circles. . . . .	39

3.4	The liquid water surface height determined via correlation with fluorescence intensity of Path 1 and 2, where Path 1 appears in the uncompressed GDL and Path 2 appears in the compressed GDL. . . . .	40
3.5	Inverted fluorescence images showing the liquid water breakthrough location with respect to the compression O-ring, where all trials except for Trial 3 and Trial 5 resulted in breakthrough originating in the area above the compression O-ring. Red arrows indicate where breakthrough coincided with the compression region. The blue arrows indicate where excess fluid exited through the outlet hole, post-breakthrough.	41
3.6	SEM images of a Toray TGP-H-060 GDL with 10 wt. % PTFE treatment before compression at (a) 200x magnification with a hand-held 1 cm x 1 cm sample (inset), (b) 800x magnification, and (c) enlarged image of (b) at 4,000x magnification. . . . .	42
3.7	SEM image of a Toray TGP-H-060 GDL with 10 wt. % PTFE treatment after it was compressed for five minutes at 0.18 MPa at 1000x magnification showing the damaged PTFE coating. . . . .	43
3.8	SEM images of Toray TGP-H-060 GDLs at 200x magnification after five minutes of compression at (a) 0.18 MPa, (b) 0.36 MPa, (c) 0.68 MPa, and (d) 1.37 MPa. Each image shows a different GDL sample. . . . .	44
4.1	Simulated gas flow channel apparatus: (a) photograph of the gas flow channel apparatus on fluorescence microscope stage, and (b) schematic showing the apparatus cross-section. . . . .	54

4.2 Dynamic water transport behaviour through an initially dry GDL: (a) liquid water pressure showing the time periods in which single droplets emerged and detached from the GDL surface and in which slug formation led to channel flooding, and (b) tracking the growth of three different droplets (A, B, and C, which correspond to times shown in (a)) (t=0 corresponds to incipient droplet formation). Raw fluorescence images are shown inset for the  $t_{i1}$  case at times indicated. Length bar indicates 0.5 mm. . . . . 55

4.3 Top view raw fluorescence images (white areas indicate location of liquid water) captured with a 2 m/s air flow velocity at (a) t = 33:01 min showing the saturated pore immediately prior to droplet emergence, (b) t = 33:03 min showing a droplet sitting above the saturated pore, and (c) after several droplet emergence/departure cycles showing a large droplet pinned to the GDL surface to the left of an emerging droplet. The air flow direction is from right to left, and the length bars are 0.5 mm long. . . . . 56

4.4 Time series of fluorescence images showing the recession of a droplet formed above the previous breakthrough location. A new breakthrough location has emerged in the lower right hand corner of field of view. The images have been inverted for clarity, and length bars represent 0.5 mm. . . . . 57

4.5 Volume of fluid (VOF) simulation results: (a) schematic showing the computational domain of the gas flow channel with two GDL pores (channels A and C), and (b) time series of VOF simulation results showing the primary filling of the smaller channel (A) followed by the secondary filling of the larger channel (C). (Red represents liquid water, and gray represents air.) . . . . . 58

5.1	Schematic showing pore network modelling results with respect to PEMFC geometry: (a) diagram of a PEMFC, (b) sample numerical pore network breakthrough pattern of a simulated GDL, and (c) SEM image of a Toray TGP-H-060 GDL (length bar represents 200 $\mu\text{m}$ ). . . . .	68
5.2	Flow diagram illustrating the pore network design and fabrication procedure. . . . .	69
5.3	Schematic illustrating various methods to construct a microfluidic pore network: (a) randomly perturbing a regular lattice of square obstacles, (b) sequentially placing square obstacles in random locations, and (c) sequentially placing square obstacles of varying sizes in random locations.	70
5.4	Perturbation procedure for generating a photomask: (a) regular square lattice, (b) translation of regular lattice in both the horizontal and vertical directions, (c) uniform distribution of horizontal and vertical translations, (d) resulting arrangement of random pore network, (e) throat width distribution, and (f) hydraulic throat radius distribution.	71
5.5	Procedure for generating a photomask for a pore network with a prescribed radial gradient: (a) regular square lattice, (b) radial translation of individual square obstacles, (c) network with radial gradient, and (d) random perturbations applied to the network with a radial gradient.	72
5.6	Comparison of numerical and experimental random pore network flow patterns at breakthrough: (a) isotropic perturbations, (b) diagonally biased perturbations, (c) radial gradient, and (d) checkerboard pattern with multiple radial gradient patches. Each numerical and experimental result comparison is accompanied by a photomask schematic with a reduced number of obstacles for clarity (along left column). . . . .	73

- 5.7 Dependence of saturation on increasing radial gradient for a 100 x 100 numerical pore network. The radial gradient is normalized by the average throat width ( $30 \mu\text{m}$ ). Filled squares represent single realizations, where empty squares represent an average value over 100 stochastic realizations with the standard deviation marked with error bars. The shaded region of the plot shows the expected range of saturation values. 74

# Acknowledgements

I would like to thank all of the teachers in my life, who have inspired and encouraged me to ask questions. They taught me to love learning, and without that, I would not be where I am today. Dr. Ned Djilali and Dr. David Sinton have been incredible supervisors and teachers throughout my graduate studies, and I will always be deeply thankful to them for their mentorship. I would also like to thank Dr. Simon Liu for his supportive co-supervision during my doctoral studies.

I would like to thank the members of the Computational Fuel Cell Engineering Group (CFCE), Microfluidics Group, and Institute for Integrated Energy Systems (IESVic). I appreciate having had the opportunity to work with such a wide range of talented students, staff and researchers. In particular, I would like to specially thank Dr. Jay Sui and Dr. Slava Berejnov for their guidance and collaboration, and Jason Heinrich, who worked under my supervision as a undergraduate researcher.

I am very thankful for the privilege of pursuing this engineering education, which has been made possible largely through the financial support of: Canada and Saskatchewan student loans and scholarships from the Natural Sciences and Engineering Research Council (NSERC), National Research Council (NRC), University of Saskatchewan, and University of Victoria.

I would also like to thank my family in Saskatchewan, including my parents, Anne and Tom, and brother, Tim, for being an unending source of encouragement and inspiration throughout my academic adventures. Last but not least, loving thanks go to my husband, Jason Bazylak, for his constant overflowing support and encouragement.

*To my mother*

# Chapter 1

## Introduction

### 1.1 Background & Motivation

In the polymer electrolyte membrane fuel cell (PEMFC), hydrogen is introduced at the anode, and oxygen is introduced at the cathode, as shown in Fig. 1.1 at the end of this chapter. These gases travel through the gas distribution channels of the bipolar plates and diffuse through the gas diffusion layer (GDL) to reach their respective catalyst layers, where electrochemical reactions of hydrogen oxidation and oxygen reduction occur. The fibrous and porous nature of a typical GDL material can be seen from the example shown inset of Fig. 1.1. The catalyst layers are separated by a thin membrane impermeable to gas but permeable to water and protons. Inlet gases, hydrogen and oxygen, are typically humidified so that when they reach the catalyst layer, they help hydrate the membrane to ensure ionic conductivity. At the anode, hydrogen splits into protons and electrons, and while protons travel through the membrane, electrons travel through an external load to reach the cathode. At the cathode, oxygen combines with these electrons and protons to produce water and heat.

The successful operation of the PEMFC relies on water management. An inad-

equivalent amount of water in the fuel cell can lead to membrane dehydration, which can accelerate membrane degradation, such as holes, that could potentially lead to fuel cross-over [1]. However, excess liquid water in the GDL can lead to flooding, a situation in which reactant gases are restricted from reaching the catalyst sites [2, 3]. Flooding in the gas channels also inhibits gaseous transport, in addition to causing non-uniform reactant distributions and parasitic pressure losses. Further losses could be introduced by the hindrance of waste heat in a flooded GDL [4]. Fuel starvation can also lead to severe electrocatalyst degradation through cell reversal [5]. The presence of liquid water also leaves the fuel cell vulnerable to further mechanical degradation resulting from ice formation and operation at sub-freezing temperatures [4, 6].

The accumulation and transport of liquid water has a major impact on the performance and durability of the PEMFC [7]. The work presented in this thesis was motivated by the need for a better understanding of the liquid water transport mechanisms in the PEMFC GDL. Specifically, this work was motivated by the need for a theoretical framework for liquid water transport in the GDL, which could lead to new GDL designs for improved water management and an overall improvement in PEMFC performance and durability.

Since the GDL consists of void volumes with microscale dimensions, it is important to consider the forces and timescales that govern the multiphase flows in this material. The Bond number ( $Bo$ ) is the ratio of body forces to surface tension forces, and is given by:

$$Bo = \frac{\rho g L^2}{\sigma} \quad (1.1)$$

Where,  $\rho$  is the fluid density,  $g$  is the acceleration of gravity,  $L$  is the characteristic length scale, and  $\sigma$  is the surface tension. On the microscale where  $L \sim \mu\text{m}$ ,  $Bo \ll 1$ , indicating that interfacial forces dominate over the influence of gravity. The capillary number ( $Ca$ ) is also an important number in characterizing multiphase flows, and is

given by:

$$Ca = \frac{\mu v}{\sigma} \quad (1.2)$$

Where,  $\mu$  is the fluid's dynamic viscosity, and  $v$  is the fluid velocity. The capillary number is a ratio of the viscous forces to surface tension forces. For the most part, the liquid flows associated with transport in the GDL are expected to be quite slow ( $v \ll \text{mm/s}$ ), resulting in low capillary numbers, which indicate the dominance of surface tension forces. The Weber number ( $We$ ) is the ratio of inertia to surface forces, and is given by:

$$We = \frac{\rho v^2 L}{\sigma} \quad (1.3)$$

During fluid propagation in the GDL, fluid flows are expected to be slow, thus the low capillary and Weber numbers. It is important to keep in mind that when liquid water completely percolates through the GDL to form a droplet (termed *break-through*), the momentary rapid expansion of this droplet is governed by a dominance of inertial forces over body and viscous forces. However, the majority of the analysis presented in this work is concerned with the transport behaviour leading up to and following the moment of breakthrough, where surface tension forces dominate.

## 1.2 Contributions

The work presented in this thesis resulted in two publications [8,9] and one manuscript [10] recently accepted in the area of investigating liquid water transport behaviour in the PEMFC GDL. The specific contributions are summarized in the following list:

**GDL compression effects on liquid water transport**

- An experimental apparatus for investigating the liquid water transport behaviour in a compressed GDL is presented.
- GDL compression results in the irreversible degradation of the GDL with a severity that is proportional to the applied compression pressure.
- GDL compression damage consists of fiber and PTFE coating breakage and deformation.
- The compression of a PEMFC GDL has a large influence on liquid water transport behaviour.
- Compressed regions of the GDL provide preferential pathways for water transport and breakthrough.

**Dynamic liquid water transport**

- A simulated cathode gas channel is presented to investigate the dynamic behaviour of droplet emergence and detachment.
- The emergence and detachment of individual droplets on an initially dry hydrophobic GDL is typically followed by slug formation and channel flooding.
- The contact line defining the saturated pore of an emerging droplet in a GDL is significantly smaller in an initially dry GDL, than in a GDL that has been exposed to several droplets.
- The GDL surface becomes prone to droplet pinning after it has been exposed to droplet emergence and detachment for a period of time.
- Droplets emerge from preferential locations in the GDL, but these locations change over time.

- Due to the observation of changing breakthrough locations, it is proposed that water transport in the GDL consists of a dynamic and interconnected network of water pathways.
- Numerical results from an idealized test system simulating the filling behaviour of liquid water within two competing pathways is presented.

### **Pore network designs for directed water transport in GDLs**

- Two-dimensional porous networks are designed with diagonal and radial biasing of void and solid volumes.
- Two-dimensional invasion percolation with trapping model predictions of capillary transport in these designed pore networks are presented.
- Experimental microfluidic pore networks are presented to provide validation for the pore network designs.
- The application of radial biasing to a random pore network results in a significant decrease in network saturation.
- The design of porous media for directed water transport is proposed for improved GDL designs.

## **1.3 Organization of the Thesis**

This thesis is organized into six chapters. The background and motivation are presented in Chapter 1, along with an overview of the contributions of the thesis. In Chapter 2, a literature review provides the background context for the contributions of this thesis. The literature review covers techniques that have been applied to visualize water in an operating PEMFC, the impact of compression on PEMFC

performance and material degradation, and the use of pore network modelling for simulating flows in porous media. The effects of compression on liquid water transport and microstructure of a PEMFC GDL is presented in Chapter 3. The dynamic behaviour of droplet emergence and detachment in the GDL is presented in Chapter 4. In Chapter 5, numerical pore network designs with experimental validations are presented, as well as a discussion of how these designs are promising techniques for directed water transport in GDLs. Finally, conclusions and future avenues of research are presented in Chapter 6. In this work, the figures and tables are provided together at the end of the associated chapter.

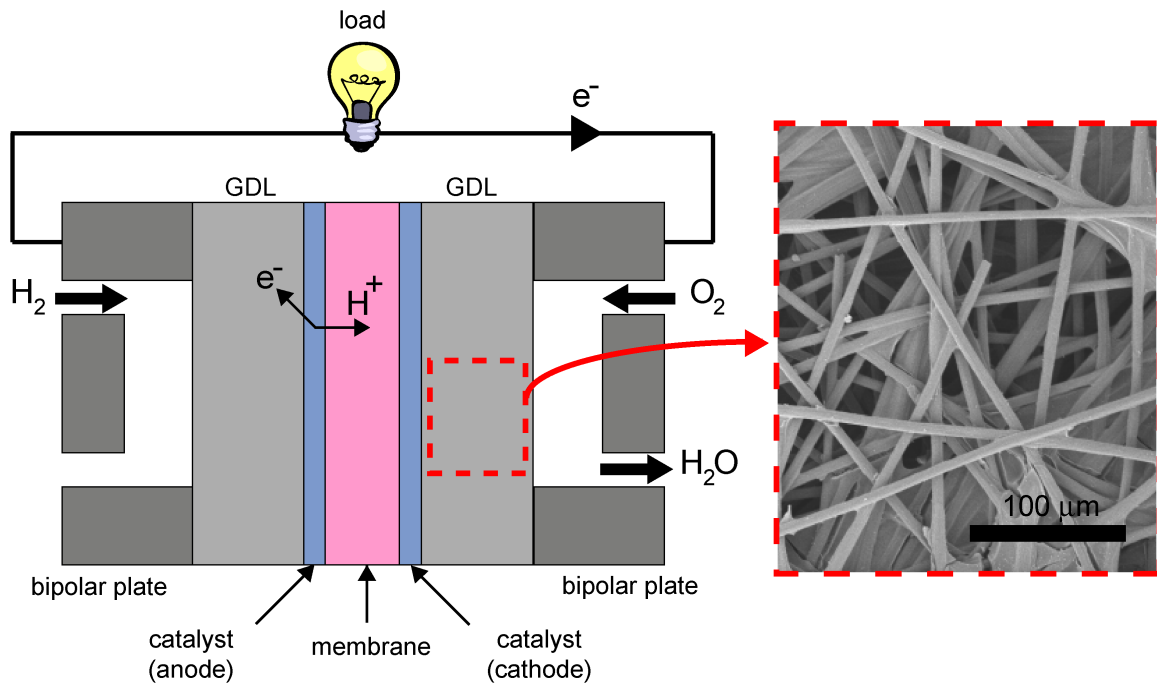


Figure 1.1: Schematic of a PEMFC. Hydrogen and oxygen diffuse through the GDLs and react at the catalyst layers. Protons released from the anode reaction travel through the ion conducting membrane, and electrons released travel through an external load. The electrochemical reactions at the anode and cathode drive the operation of the fuel cell by producing an electric potential and a current through an applied load. A Toray TGP-H-060 GDL is shown inset, outlined by a dashed red line.

## Chapter 2

# Literature Review

Within the last few years, empirical methods have been employed extensively to analyze the water distribution in fuel cells and to correlate this water accumulation to performance. These works were motivated by the detrimental impact that poor water management has on efficient fuel cell performance. In addition to water management, the compressive pressures associated with cell assembly also have an impact on performance. Empirical methods, such as those employed to investigate water transport and compression in the fuel cell, have the potential to provide useful feedback for empirical correlation development and/or validation of theoretical models [11]. For instance, these empirical results could provide feedback and validation for the development of a GDL representative pore network model. In this chapter, a literature review is provided of i) the techniques that have been applied to visualize liquid water in an operating PEMFC or simulated fuel cell conditions, as well as the hypotheses that have been proposed to describe liquid water transport in the gas diffusion layer (GDL), ii) the impact of compressive loads on PEMFC performance and material degradation, and iii) the application of pore network modelling for multiphase transport in porous media, as well as recent applications to modelling transport in the GDL.

## 2.1 Liquid Water Visualization

In this section, an overview will be provided for the following visualization techniques: nuclear magnetic resonance (NMR) imaging, beam interrogation, and direct optical photography. Liquid water transport in an operating PEMFC is a challenging phenomenon to study using *in situ* visualization techniques, due to the opaque nature of traditional bipolar plate materials. NMR imaging [12–24] and beam interrogation techniques, such as neutron imaging [4, 25–32], electron microscopy [33, 34], and x-ray techniques [35, 36], enable the *in situ* measurement of liquid water distributions in operating PEMFCs through materials that would otherwise be opaque to optical access. However, the direct optical visualization [7, 8, 37–45] of liquid water in PEMFCs and PEMFC materials has the potential to provide high temporal and spatial resolution information about water transport in the gas flow channels and upper layers of the GDL. Table 2.1 summarizes the reported spatial and temporal resolution of the methods discussed in this section.

This review focuses on several visualization techniques for measuring the liquid water distribution in operating PEMFCs and PEMFC materials. However, there are various other methods that have been applied to measure PEMFC water content, such as gas chromatography [46], ionic resistance [47], infrared absorption [48], residence time distribution [49, 50], etc. These methods will not be described in detail here; however, St-Pierre provides a broad overview of *in situ* water measurement methods in [51].

### 2.1.1 Nuclear Magnetic Resonance (NMR)

In nuclear magnetic resonance (NMR) imaging, otherwise known as magnetic resonance imaging (MRI), the quantum mechanical magnetic properties of an atom's nucleus are exploited to provide image contrast. In NMR imaging, specific atomic nuclei with non-zero spin moments, such as  $^1\text{H}$ , are excited by a static magnetic field

and a radio-frequency signal. The excited nuclei absorb this radio-frequency energy and resonate at a detectable frequency that is proportional to the strength of the applied magnetic field [51]. By measuring the emitted radio-frequency signal from excited  $^1\text{H}$  nuclei in a fuel cell, the presence of water molecules can be detected. NMR imaging provides a useful tool for measuring the liquid water distribution of an operating fuel cell *in situ*, where liquid can be detected under the gas channel land areas, in contrast to direct optical photography.

In 2004, Tsushima et al. [12] reported the use of NMR imaging to measure the spatial distribution of water in a 340  $\mu\text{m}$  thick Nafion membrane of an operating PEMFC. They correlated this water content with the output current density of the cell at steady state operation. They performed NMR imaging of the PEMFC through-plane and observed a lesser amount of water at the anode compared to the cathode side, which they attributed to the dominance of the electroosmotic drag of water over back diffusion.

In the same year, Feindel et al. reported the use of NMR imaging to examine the distribution of water in an operating PEMFC [13]. In contrast to the work of [12], Feindel and co-workers imaged the in-plane direction of the PEMFC. They observed a radial gradient of water distribution, and reported the diffusion of liquid water from the membrane electrode assembly (MEA) into the surrounding Nafion membrane.

In 2005, Tsushima et al. employed NMR imaging to investigate the performance of a PEMFC with a direct liquid water supply to the membrane [14]. They found that the use of a direct water supply to the membrane resulted in an increase in cell voltage, which they attributed to the decrease in membrane resistance. From NMR imaging, a deformation in the PEM was observed where the water supply came into contact with the membrane. They attributed this deformation to the localized swelling of the membrane. This group also measured membrane water content to investigate the effect of changing membrane materials [15, 24] and membrane thickness [16]. In a separate work [17], these authors employed their NMR imaging results of the PEM

through-plane to validate the development of a one-dimensional model for PEM water transport.

Minard et al. [18] employed NMR imaging to the in-plane direction of a PEMFC and observed the formation and slow propagation of a dehydration front from the gas inlet side to the gas outlet side of the cell over 11 hours of continuous operation. Feindel and co-workers [19–21] also performed further investigations of in-plane water distributions in the PEM. They found that the water content and performance of the fuel cell were sensitive to the gas flow configuration of the cell. In particular, they reported that counter-flow configurations resulted in more uniform PEM water distributions [19]. These authors also demonstrated the employment of hydrogen-deuterium exchange as a method of providing contrast in NMR imaging to investigate changes in PEM water distributions during steady-state conditions [22].

Although NMR imaging provides useful information about the water content in the gas channels and membrane, there are several drawbacks to this method, including poor temporal resolution (50 s [12]), spatial resolution ( $400\ \mu\text{m} \times 25\ \mu\text{m}$  [12]), and invasiveness due to changes in fuel cell materials (nonmagnetic current collectors, such as acrylic resin [16]). The limiting size of the magnet-core for fuel cell housing is also a drawback [51]. For instance, typically small single cells accompany NMR based investigations, such as that utilized by Tsushima et al., where a  $2.0\ \text{cm}^2$  was employed [12]. Furthermore, NMR imaging cannot be used to resolve water content in the GDL due to the rapid attenuation of the signal in the carbon layer [21, 35].

## 2.1.2 Beam Interrogation

### Neutron Imaging

Neutron imaging relies on the measurement of an attenuated signal after a sample has been bombarded with a neutron beam. The attenuation of the signal is proportional

to the material composition. This method is particularly useful for PEMFCs due to the neutron's sensitivity to hydrogen containing compounds, such as water [25], and insensitivity to common fuel cell materials (for example, aluminum and graphite) [20]. Due to high costs and limited availability of neutron imaging, this research has been concentrated amongst a few groups worldwide [51], including the National Institute of Standards and Technology's Center for Neutron Research (NIST CNR) [25, 29, 30, 52–58], the Penn State Breazeale Nuclear Reactor [4, 28, 31], and the Paus Scherrer Institut (PSI) [26, 27, 32].

In 1999, Bellows et al. [52] reported the first use of neutron imaging to measure water content in an operating PEMFC. They demonstrated the ability to measure the response of water content in the membrane with respect to changes in gas humidification levels. Xu et al. [59] also performed imaging along the fuel cell through-plane to investigate water distribution in the membrane.

In 2004, Satija et al. [25] employed in-plane neutron imaging of an operating PEMFC and produced a time series of images to evaluate the water management of a fuel cell system. Neutron imaging has since been used extensively to visualize water accumulation along the in-plane direction to observe a two-dimensional distribution of water [28, 29, 54, 60, 61]. Pekula et al. [28] reported the tendency for liquid water to accumulate at the 90° bends in the gas channels. The authors attributed this to the change in momentum of the gas flow, which resulted in localized pressure variations. Similar results were reported by Trabold et al. [29], as they also observed the accumulation of liquid water at the channel bends. However, they postulated that this behaviour could have been influenced by the higher degree of fuel cell assembly clamping pressure at the edges, in conjunction with the channel bend locations. Hickner and co-workers [54] investigated the water content in the PEMFC as a function of current density and temperature. They reported that water content decreased with increasing temperature, and they attributed this to the evaporation of liquid water at higher temperatures. Recently, Li et al. [61] employed neutron imaging in the

through-plane to evaluate flow channel designs.

Several authors have also employed neutron imaging to specifically focus on measuring the liquid water distribution in the cathodic flow fields and GDL [4, 27, 30–32, 53, 55, 56]. Kramer et al. [27] studied the effect of varying flow field geometries on water distribution, and they reported that the cathodic GDL was prone to water accumulation. Zhang et al. [32] employed neutron imaging to investigate the effect of changing the cathodic GDL material on liquid water accumulation in a single cell. They reported that a cloth GDL tended to accumulate less water than paper GDLs. Kowal and co-workers [4] quantified the liquid water distribution in a PEMFC under varying flow rates, humidities, and currents for both paper and cloth GDLs, and they found that paper GDLs held 174 % more water per volume under the land area in comparison to cloth GDLs, which ultimately led to a comparatively poorer performance. Owejan et al. [30] observed that the cathode flow channels retained less water when the reactant flow and current density increased. Turhan et al. [31] visualized water in the channels and GDL, and observed the tendency for water to accumulate under the land area more than under the channels.

In the past, neutron imaging typically provided a spatial resolution of  $100\ \mu\text{m}$  x  $100\ \mu\text{m}$ , which was insufficient to analyze the through-plane evolution of water transport. Difficulties in distinguishing the presence of water in the GDL from water in the flow channels have been reported [4, 62]. Furthermore, typical integration times (1.0 s) for this technique are also insufficient to measure the microscale transport of droplet movement in a fuel cell, which has associated time scales of milliseconds [51]. However, the National Institute of Standards and Technology (NIST) has recently demonstrated the capability of imaging with a spatial resolution of  $25\ \mu\text{m}$  [58], and work conducted at the Penn State Breazeale Nuclear Reactor as well as the NIST CNR was reported with frame rates up to 30 frames/s [28, 53].

## **X-ray**

In x-ray microtomography, a material is exposed to an x-ray beam, and the intensity of the signal is attenuated as it travels through the material. The transmitted signal is measured to provide a three-dimensional map of adsorption variation within a sample. Sinha et al. [35] demonstrated the use of this technique to measure the liquid water distribution in a GDL during gaseous purges at high spatial resolution ( $10 \mu\text{m} \times 10 \mu\text{m} \times 13.4 \mu\text{m}$ ).

Synchrotron x-ray radiography has recently been demonstrated by Manke et al. [36] as a high resolution measurement ( $3 - 7 \mu\text{m}$ ) technique for water distribution in an operating fuel cell. With an image acquisition time of 4.8 s, Manke and co-workers employed this technique to observe the dynamic water transport behaviour in an operating PEMFC with some through-plane resolution. They observed an *eruptive transport* mechanism [36], which they described as the quick ejection of droplets from the GDL into the gas channel.

## **Electron Microscopy**

Nam and Kaviany [33] employed an environmental scanning electron microscope (ESEM) to visualize condensed water droplets on GDL fibers in the absence of bulk liquid water transport at low temperature and vapour pressure. These authors employed consecutive images of water droplet growth on the GDL for the development of a one-dimensional water saturation model for the GDL. This method provides high spatial resolution; however the ability to simulate fuel cell operating conditions has not yet been demonstrated.

### 2.1.3 Optical Photography

Optical photography has been employed extensively to visualize liquid water transport in a PEMFC via optically accessible flow fields [7,37–40,43,44,63,64] and in simulated gas flow channels [39,41,43].

Tuber et al. [7] visualized liquid water transport in the cathode gas channel of a transparent PEMFC. They operated their fuel cell at 30°C, and found that using a hydrophilic cathode GDL resulted in increased current density, which they attributed to a more uniformly hydrated membrane. Spornjak et al. [63] also investigated the effects of varying GDL materials and hydrophobicity. They found that PEMFCs with untreated GDLs were more prone to film and slug formation in the cathode gas channel. Weng et al. [44] observed the beneficial effects of high cathode gas flow rates for water removal; however non-humidified cathode gas streams at high stoichiometry resulted in membrane dehydration. Ge et al. visualized water droplet formation in the anode gas channels, and they observed that droplets tended to form on the gas channels when a hydrophobic GDL was employed, whereas hydrophilic GDLs tended to wick water from the channel into the GDL.

Yang et al. [38] visualized water droplet emergence from the GDL surface and behaviour in the gas channel. These authors observed a variety of phenomena in the gas channel, including the intermittent emergence of droplets from the GDL surface, film formation along the channels, and channel clogging. Hakenjos et al. [37] also employed a transparent fuel cell and attempted to correlate the appearance of flow field flooding with the spatial temperature distribution. Sugiura and co-workers [40] employed a transparent fuel cell to evaluate and successfully demonstrate the mitigation of flow field flooding with the use of a water absorption layer.

Borrelli et al. [39] employed a simulated cathode gas channel to image water droplet transport through a GDL into a gas channel. Similarly to Tuber et al. [7] and Yang et al. [38], these authors observed droplet emergence at preferential locations.

However, an explanation of this phenomena was not provided. Theodorakakos et al. [43] also utilized a simulated cathode gas channel to capture side-view droplet detachment images for computational fluid dynamics (CFD) volume of fluid (VOF) simulations.

Transparent fuel cells provide useful information on how flow field flooding corresponds to current density degradation; however, the spatial resolution required to analyze the transport of liquid water within the GDL has not yet been reported. Furthermore, for the exception of Borrelli et al. [39] and Theodorakakos et al. [43], who achieved image acquisition times of milliseconds, transparent fuel cells have not been employed at sufficiently high temporal resolutions to investigate the dynamic behaviour of droplets. Kumbur et al. [41] employed a simulated flow channel apparatus to study the effects of hydrophobicity, channel geometry, droplet chord length and height, and air flow rate on droplet formation.

### **Fluorescence Microscopy**

Fluorescence microscopy in conjunction with optical photography provides a method to visualize the microscale transport of liquid water in the surface of the GDL. Lister et al. [45] directly visualized the through-plane liquid water transport in the GDL using a fluorescent tracer. A dye solution was injected through the GDL of a PEMFC, and fluorescence microscopy was employed to visualize the transport of liquid water through this fibrous structure to the extent that the opaque fiber structure would allow. The technique allowed for the tracking of time-evolving gas/liquid interfaces, and provided unique insight into the dynamics of liquid water flow through distinct pathways. Water transport at the surface was found to be dominated more by fingering and channeling, accompanied by highly dynamic eruptive water transport processes. Recent *in situ* visualizations using synchrotron x-ray radiography [36] confirm this eruptive transport process and show that this occurs during operation of some localized areas of the cell, while in others areas, GDL pores fill continuously

following the capillary tree-like process [3, 33].

### 2.1.4 Hypothesis

Although efforts have been made to model water transport in the PEMFC [65–68], until recently, little attention has been paid to develop models for microscale liquid water transport in the porous GDL. Due to the lack of two-phase flow correlations required for closure in macroscopic models, multiphase PEMFC continuum models often rely on empirical measurements of water transport in unconsolidated sand [69] for transport in the GDL.

Nam and Kaviany [33] proposed a branching-type geometry, where water vapour condenses on GDL fiber surfaces to produce micro-droplets. Micro-droplets agglomerate to form macro-droplets, followed by water flowing preferentially toward larger pores. The authors hypothesized that water is distributed in a branching geometry where large streams act as the backbone for macro-transport, and smaller streams transport water from micro-droplets to macro-droplets. Pasaogullari and Wang [3] also hypothesized the formation of a tree-like liquid water percolation in the GDL after condensation begins.

From the work of Litster et al. [45], water transport was found to be dominated by fingering and channeling, rather than via a converging capillary tree suggested in the prior work of Nam and Kaviany [33] and Pasaogullari and Wang [3]. In the hypothesis proposed by Litster and co-workers, numerous “dead ends” occur where water transport recedes when adjacent breakthrough channels form.

## 2.2 Compression Effects

Fuel cells are assembled under compressive loads to prevent gas leakages, however the degree of compression can impact the performance of the fuel cell. For instance,

under compressive loads, the GDL thickness and porosity may decrease, which could lead to higher mass transfer resistance. However, compressing the GDL could also result in decreased contact resistance with the bipolar plate. Recent experimental studies have been conducted to examine the effects of the stack assembly pressure and the compression of the GDL on PEMFC performance [70–73] and characteristics [74–77]. Recently numerical models have been introduced to model the pressure distribution in a fuel cell stack [71] and simulate the effect of compression on PEMFC performance [78–81]. Quantified compression pressures for the GDL in the literature are few and varied [75] due to the proprietary nature of fuel cell design as well as the difficulty in taking measurements. There is further ambiguity in quantifying the pressure applied to the GDL because the surface area in contact with the bipolar plates varies depending on the channel to land ratio.

Lee et al. [70] reported that PEMFC performance decreased with increasing manifold bolt torque. A torque of 100 in·lb/bolt, corresponding to 1.61 MPa inside the fuel cell, resulted in the best performance with a Toray GDL. They suspected that higher torques damaged the GDL and decreased the electrical resistivity between the MEA and the current collecting plates, but no direct experimental evidence was provided. Wilde et al. [82] also reported a decrease in the through-plane resistivity with increasing compression force. Ge et al. [72] studied how GDL compression affected PEMFC performance. They achieved the best fuel cell performance with carbon fiber paper with the smallest compression ratio of 14 %, which was achieved with approximately the weight of the collector plate on top of the GDL. From these results, they concluded that an optimal compression could not be determined because a compression that is at or below this optimal value would be inadequate to seal the fuel cell. Ge et al. suggested that most fuel cells probably suffer from over-compression. Ous et al. [73] also compared the performance of a PEMFC when varying the clamping pressure, and they found that a compression of up to 2 MPa improved the performance of the fuel cell by decreasing contact resistance between the GDL and bipolar

plate; however, increasing the assembly pressure beyond this critical point resulted in poorer performance due to increased mass transport limitations.

Ihonen et al. [74] investigated the effect of fuel cell clamping pressure on PEMFC flooding. They found that increasing clamping pressure resulted in decreased thermal resistance, contact resistance, and mass transfer for Sigracet GDL 10-BC and Carbel CL GDL materials. Escribano et al. [75] showed that stress applied to a carbon cloth GDL resulted in decreased thickness and electrical resistivity. They performed two successive compressions to carbon cloth and paper, where the first compression (0.5 MPa) represented the pressure commonly used to make the MEAs, and the second (1.5 MPa) represented the compression caused by the current collecting plates. Both carbon cloth and paper exhibited several cracks after compression. Matsuura et al. [76] investigated the effect of employing metallic bipolar plates on the structure of the GDL. In addition to measuring decreasing electrical resistance with increasing compression, they also commented on the severe damage that occurred to the GDL in their fuel cell assembly. Nitta et al. [77] investigated the effect of GDL properties due to the inhomogeneous compression caused by the channel/land structure of the flow-field plate. They found that the GDL under the channel experienced only slight compressions at high fuel cell assembly compression, while the thickness of the GDL under the land compressed significantly. Lee et al. [71] measured the pressure distribution in the MEA of a PEMFC to provide feedback for their numerical simulations of pressure distributions in a fuel cell stack.

These publications uncover the effect of fuel cell performance and GDL characteristics due to varying compression pressures; however, these studies did not specifically address how liquid water transport is influenced by this compression.

## 2.3 Pore Network Modelling

### 2.3.1 Background

In 1956, Fatt was the first to use a network of pores to model multiphase flow in porous media [83–85]. In 1957, Broadbent and Hammersley [86] introduced percolation theory. For many years following these pioneering works, the field of two-phase flow through porous media received little attention [87]. Adler [87] provided a good review on the development of percolation theory applied to multiphase flow. In the late 1970’s, Levine et al. [88], Larson et al. [89], and DeGennes and Guyon [90] almost simultaneously put forth the idea to analyze two-phase flow in porous media using percolation theory [87].

Percolation theory is the study of clusters that are formed when a very large lattice is occupied with a random probability [91]. At a critical probability, a cluster extends from the top to bottom and left to right of a square lattice [91]. This cluster is called the percolating cluster [91]. The percolation process is defined as the spread of a fluid through a medium under the influence of a random mechanism associated with the medium, as opposed to the diffusion process, which is the random mechanism associated with the fluid [86,92].

In 1982, Chandler et al. [93] from the Schlumberger-Doll Research group, published their numerical results of two-phase porous media flows. They investigated the quasi-static stepwise displacements of one fluid by another fluid in a finite two-dimensional lattice. From the same research group, Lin and Cohen [94] modelled porous Berea sandstone as a network of pores connected by throats or channels. In the extended work of the Schlumberger-Doll Research Group, Wilkinson & Willemssen [95] coined the name “invasion percolation” [87]. In invasion percolation, the displaced fluid is called the “defender” and the injected fluid is called the “invader”. Here, a trapping rule is used, where after a defending fluid forms an isolated clus-

ter, the invading fluid cannot penetrate this cluster. With percolation theory, the displacement process is caused by a constant applied pressure, and the interfaces are advanced to a prescribed threshold resistance [95]. In contrast, for invasion percolation, the displacement process is driven by a constant flow rate, and the interface is advanced at the point of least resistance in the network. The case that applies to the oil industry is where a less viscous fluid is used to displace a more viscous one, such as oil [95]. If oil becomes trapped in clusters, the less viscous fluid cannot displace it. Retrieving the residual oil left in the ground is of significant importance in oil recovery.

Since the early development of pore network modeling [83–86], models with spatially homogeneous pores and throats have been employed to study the displacement processes in idealized porous media [95]. Over the past two decades, network models have been applied to a multitude of areas ranging from rock physics [94], oil recovery [93, 96–100], ground water hydrology [101], textile characterization [102], etc. Blunt [103] provides a broad review of recent pore network model developments.

Experimental validation has been provided for theoretical pore network models [104–114]. Recently, Berejnov et al. [115] presented a lab-on-chip approach to study two-phase transport in porous media, employing microfluidic rapid prototyping fabrication methods in conjunction with fluorescence microscopy to study water transport in pore networks. Experimental network results have also been used in other porous media applications to guide and validate theoretical modeling [116, 117] or as inputs to existing models [118]. Microfluidic networks were applied as a validation technique in this thesis.

Pore network models provide an alternative to continuum phase models to elucidate transfer phenomenon and determine transfer parameters in porous media. Continuum modeling of porous media becomes unattractive when the porous media has a complex three-dimensional heterogeneous and disordered geometry. Numerically tracking phase interfaces and calculating surface tension forces becomes computa-

tionally expensive. Alternatively, discrete pore network modeling is an intermediate approach where the disordered porous media is represented by an equivalent network of pores and throats, and phase transport is dominated by percolation theory. By using this computationally-efficient discrete approach, a statistical analysis can be performed by randomizing the network model to more accurately represent the disordered porous media.

In pore network modeling, the media is mapped into a set of interconnected pores and throats, and the throats are assigned varying hydraulic conductivities. In capillary dominated flows (such as slow drainage), a simplified displacement criterion can be implemented. In the invasion percolation with trapping model, the throat with the largest conductivity at the interface is invaded by the invading fluid at each discrete step. The invasion process is stopped once fluid appears in one of the outlet boundary throats. The conservation of mass is calculated for each pore in the network, producing a set of linear equations that are used to solve for pore pressures. A network realization produces a static configuration of the invading phase pattern. Each network realization is deterministic, which means the static invading phase pattern is determined by the throat size distribution of the network.

To characterize the transport of non-reactive and non-conductive two-phase-flow, the characteristics of porous media of interest are: thickness, geometry, length scales, mean pore size, pore size distribution, porosity, single phase permeability, and phase permeability. (For more complex problems, compressive behaviour, thermal resistance, electric resistance, chemical resistance, strength, etc. may also be of interest.) The fluid properties, viscosity, density, and surface tension, also determine the flow behaviour. Experimental methods can be used to determine the physical characteristics of the porous media. For example, microscopy can be used to determine the medium thickness and geometry, length scales of pores, and pore shape. Porosimetry can be used to measure the mean pore size, pore size distribution, and porosity of the material. Microscopy can also be utilized to determine the coordination number of

the medium (connectivity), which is equal to the ratio of connected pores to the site pore in the network model. In two-dimensional pore network modeling, the medium thickness and geometry are used to determine appropriate boundary conditions. For the case of in-plane transport, a square geometry is used with no-flow boundary conditions on the left and right sides. The invading fluid enters the network at one side (inlet) and flows out the opposite side (outlet). The length scales of the medium are used to define the throat lengths. The mean pore size and pore size distribution are translated into the mean throat size and throat size distribution, respectively. The porosity and fluid properties are used directly in the model. Pore network modeling can then be used to determine single phase permeability, and more importantly, the relationships between phase permeability and saturation under different operating conditions (inlet pressure, invaded and invading fluids, and temperature, etc.)

### **2.3.2 Application of Pore Network Modelling to the GDL**

The majority of pore network models have been applied to enhanced oil recovery applications [96, 99, 119, 120] with the porous medium being sand or rock. Since more than 50 % of the original oil is left entrapped in the pores of the oil-bearing sand or rock [96, 119], a large body of work focuses on mobilizing entrapped oil ganglia. In contrast, the application of pore network modeling of water transport in the GDL is unique because the porous medium is hydrophobic and has an entirely different geometry. In the GDL, the porosity is generated from pressed cylindrical fibers, which are covered with a hydrophobic layer. A common goal in using pore network modeling in the GDL is not to mobilize a certain trapped phase, but rather to understand the relationship between relative permeability and capillary pressure on invading phase saturation. With an understanding of how the physical parameters affect these relationships, the GDL can be more accurately modelled in continuum fuel cell models.

Empirically determined characteristics of the GDL (such as pore size distribution, contact angle, and morphology) can be employed to develop GDL-representative pore network models. In fact, the pore network modeling approach has been very recently extended to the GDL by Gostick et al. [121], Markicevic et al. [122] and Sinha and Wang [123]. Markicevic et al. [122] used network simulations to investigate and establish the functional dependence of the relative permeability and capillary pressure on liquid water saturation, two of the key parameters required for two-phase PEMFC models [2]. Significant improvements in the PEMFC are contingent on advancements in water management, particularly in the GDL. Unfortunately, conventional GDLs are considered ineffective for water removal and organized water transport due in part to its arbitrary structure [124], and excess water can reduce transport of reactant gases [2] as well as exacerbate degradation [5]. To mitigate these water management issues, new methods for enhanced water transport have been demonstrated via the active removal of water through the use of transport plates [125] and electroosmotic pumping [126, 127]. However, one potential avenue for improving water management is the development of GDL materials engineered for improved water management at the microscale. The use of pore network modelling provides a novel technique for designing new GDL materials.

Table 2.1: PEMFC visualization methods: summary of resolution capabilities.

Method	Spatial Resolution	Temporal Resolution	Ref.
NMR	25 $\mu\text{m}$	50 s	[12]
Neutron Imaging	100 $\mu\text{m}$	1.0 s	[25]
Synchrotron x-ray	3-7 $\mu\text{m}$	4.8 s	[36]
Microtomography	10 $\mu\text{m}$	0.07 s	[35]
Optical photography	10 $\mu\text{m}$	2.0 s	[38]
Fluorescence microscopy	5.38 $\mu\text{m}$	0.1 s	[8, 45]

## Chapter 3

# GDL Compression Effects

The focus of this chapter is the investigation of the effect of compression on liquid water transport and on the microstructure of PEMFC GDLs. The effect of GDL compression on liquid water transport is potentially important because of the intricate relationship between pore radii and surface tension on the transport properties of the GDL [128]. The influence of compression on water breakthrough locations in the GDL is investigated here by placing the GDL in an optically transparent clamping apparatus and employing fluorescence microscopy to visualize liquid water transport. Scanning electron microscopy (SEM) is also employed to study the effects of compression on the morphology of the GDL. This work brings new insight on the influence of distribution channels on the development of GDL flooding, and documents the structural changes in the GDL due to compression.

### 3.1 Experimental

Fluorescence microscopy was utilized to visualize liquid water transport in the through-plane of a GDL. Fluorescence based visualization takes advantage of the following three-step process in which molecules that exhibit fluorescence experience the ab-

sorbance, dissipation and emission of energy [129]. The fluorescent dye employed in this work, fluorescein (MW 332.31), has a maximum absorbance of 490 nm (blue light) and a maximum emission wavelength of 513 nm (green light). A dilute solution (1 mM) of fluorescein was used to tag the liquid phase, as it traversed through the plane of the GDL. This dilute fluorescein dye solution (83 ppm) has negligible effects on the properties of water [130]. All wavelengths below the expected emission spectrum were filtered, and the intensity of the light detected was correlated to the height of the liquid.

### 3.1.1 Gas Diffusion Layer

For all of the studies reported in this paper, a Toray TGP-H-060 non-woven fibrous GDL material was used. This particular material was chosen for investigation because it is commonly used in fuel cell testing and is a readily available commercial product. The GDL must provide a path for product water to be removed from the catalyst layer. In order to facilitate water transport and alleviate potential flooding, the GDL is generally made hydrophobic in its bulk [128]. In practice, the GDL is commonly coated with a solution of polytetrafluoroethylene (PTFE) to increase its hydrophobicity. In particular, the GDL material studied here had a PTFE content of 10 wt. %. The Toray TGP-H-060 GDL is also a highly porous media with more than 50 % of its pore sizes ranging from 30 - 40  $\mu\text{m}$  [131], with a thickness of 190  $\mu\text{m}$  [131], and a mean fiber diameter of 8  $\mu\text{m}$  [45].

### 3.1.2 Apparatus

Fig. 3.1 shows the schematic of the fluorescence microscopy and GDL clamping apparatus. The GDL was clamped above the fluid reservoir and a compression O-ring, which compressed the GDL and prevented leakage. A Plexiglas top plate with a hole in the center of diameter,  $d = 2$  mm, (for liquid to escape) was clamped above the

GDL with eight screws. An optical microscope was used to perform the fluorescence microscopy, and images were captured with a charge-coupled device (CCD) camera (QImaging Retiga 1300i Cooled Mono 12bit). A programmable syringe-pump (Harvard Apparatus PHD 22/2000) was used to deliver the fluorescein dye via Teflon FEP tubing (Upchurch Scientific, WA) from the syringe pump to the GDL at a rate of 0.02 mL/min. Normalized by the GDL planar area considered, and assuming no net water transport between anode and cathode, this water flow rate would correspond to high current densities [41]. The capillary number ( $Ca$ ) and Weber number ( $We$ ) are of the order of  $10^{-7}$  and  $10^{-10}$ , respectively, indicating the dominance of surface tension forces and relative insensitivity to momentum and flow rate.

### 3.1.3 Data Acquisition

Transient images were captured with an optical microscope (Leica Microsystems DML) with a cooled CCD camera. The results in this paper were obtained with a 1.25x magnification objective exhibiting a numerical aperture,  $NA$ , of 0.04. The theoretical depth of field is  $321 \mu\text{m}$  as calculated by the following expression, where  $\lambda$  is the wavelength of emitted light (513 nm).

$$d_{field} = \frac{\lambda}{NA^2} \quad (3.1)$$

The 1.25x magnification lens was used because it provided sufficient resolution of the liquid water and provided a viewing region that included the compressed regions of the GDL. Larger magnification lenses would have resulted in higher local resolution, but at the expense of a smaller viewing region. As the goal here was to ascertain the effect of compression on the GDL, a suitably large area was required to achieve a representative sample of the material. With pore sizes on the order of 30 - 40  $\mu\text{m}$  [131], the circle defined by the compression ring's inner diameter (4 mm) corresponded to

approximately  $1 \times 10^6$  to  $1.8 \times 10^6$  pores and was thus assumed to provide a reasonable representation of this material.

As proposed by Litster et al. [45], the fluorescence intensity field can be correlated to the through-plane height of the liquid water. The observable vertical depth presented herein is  $100 \mu\text{m}$ , which is less than the theoretical depth of field because of the opacity of the GDL. The observable depth of field was supported by observations of fluorescein within the height of seven  $8 \mu\text{m}$  fiber diameters and the observation of flooding above the surface of the GDL into the hole of the top plate. This depth of field resulted in the following 8-bit linear intensity correlation,  $\eta$ , where  $I$  is the 8-bit intensity data.

$$\eta = \frac{100\mu\text{m}}{255}I \quad (3.2)$$

Ideally, a high frame rate is required for a thorough analysis of the fluorescein propagation. But, since higher frame rates arrive at the cost of reduced pixel resolution, images were captured at a frame rate of 3.25 frames/s. Binning the images resulted in a decrease in spatial resolution, but an increase in temporal resolution. The frame rate was chosen to maintain the lowest spatial resolution required for this analysis. This frame rate was achieved with a spatial resolution of  $21.4 \mu\text{m}/\text{pixel}$ . The Hitachi S-3500N Scanning Electron Microscope (SEM) was used to investigate the morphological changes in the GDL before and after compression of varying pressures.

### 3.1.4 Results & Discussion

#### Effects of Compression on Liquid Water Transport

The GDL clamping apparatus shown in Fig. 3.1 was used to clamp the GDL at a prescribed pressure of 1.5 MPa, using eight screws, each with a torque of 2 in·lb.

The compression pressure was calibrated using a pressure indicating film (Pressurex, Sensor Products LLC, NJ). The film with a range of 0.48 - 2.41 MPa was inserted between the O-ring and the top clamping plate. As pressure was applied, microcapsules in the film were released providing a colour whose intensity directly related to the amount of applied pressure. The compression pressure used here is comparable to the pressures reported by Lee et al. (1.61 MPa) [70] and Escibano et al. (0.5 MPa and 1.5 MPa) [75].

The transport of water through the GDL, both in operating fuel cells and this experiment, is punctuated by liquid water breakthrough events which are due to liquid water pressure accumulation under the GDL. In these experiments, the location of liquid water breakthrough is of interest, rather than the behaviour of liquid water transport post-breakthrough. Thus, the dye injection rate was less important than the pressure at which the dye emerged from the surface of the GDL. As the dye was injected into the bottom side of the GDL, the pressure of the dye stream increased until a critical pressure was reached. When the dye stream reached this critical pressure, it exerted the necessary force to penetrate the GDL. The liquid water breakthrough pressure was measured with a pressure gauge (McMaster Carr) for each trial with a new sample, and is listed below in Table 3.1. The small variation in breakthrough pressures is attributed to the non-uniform fiber orientation (and thus pore size distribution) and non-uniform PTFE coating for each particular sample used.

Fig. 3.2 shows one set of time-sequenced images of the fluorescein solution traveling through the GDL at (a) 4.9 s, (b) 5.2 s, and (c) 6.5 s. The images on the left were captured with a CCD camera projected onto the top surface of the GDL and inverted for clarity to show the evolution of water transport. The dashed concentric circles indicate where the compression O-ring was placed beneath the GDL in the clamping apparatus. To the right of each image is the three-dimensional rendering resulting from the correlation between intensity and liquid surface height. This figure shows

that breakthrough occurred under the area of GDL compression, and proceeded to flood toward the center of the viewing area, where there was a hole open to atmosphere in the top clamping plate. The results shown in Fig. 3.2 are typical of the experimental trials conducted.

Two particular paths shown in Fig. 3.3 are discussed in more detail. Path 1 was the first pathway to appear during this visualization, as shown by the peak in the three-dimensional rendering in Fig. 3.2 (a). It is also important to note that Path 1 formed under the uncompressed area of the GDL, i.e. not between the concentric circles outlining the O-ring compression area. Path 2 became the dominant pathway, which formed after Path 1 at 5.2 s. Although Path 1 formed before Path 2, Path 2 became the dominant path leading to water breakthrough.

Fig. 3.4 shows the evolution of water surface height for Path 1 and 2. Liquid pressure accumulated under the GDL until the liquid exerted sufficient force on the GDL to traverse in the through-plane direction. At 0.92 s, Path 1 rose to  $6.3 \mu\text{m}$ , while Path 2 had a surface height of  $5.2 \mu\text{m}$ . For the next 4 s, the surface heights in Path 1 and Path 2 remained constant as the liquid water pressure built beneath the GDL. At 5.2 s the liquid pressure reached the critical pressure for breakthrough, and Path 2 suddenly rose to a height of  $55.5 \mu\text{m}$ . The liquid water pressure beneath the GDL (5.7 kPa) was sufficient to breakthrough the compressed GDL at Path 2 (preferential pathway), but was insufficient to breakthrough the GDL that was not compressed (Path 1).

Fig. 3.5 is the collection of inverted fluorescence images captured with the camera projected at the surface of the GDL showing the liquid water breakthrough locations with respect to the compression O-ring for ten trials, where Trial 8 has already been discussed in detail (Figs. 3.2, 3.3, 3.4). As shown, all trials except for Trial 3 and Trial 5 resulted in liquid water breakthrough originating from the compressed area. The red arrows indicate where breakthrough coincided with the compression region. The blue arrows indicate where excess fluid exited through the outlet hole, post-

breakthrough. If one assumes liquid water transport behaviour is the same in the compressed and uncompressed GDL, then statistically 44 % of the breakthroughs should have occurred in the area defined by the compression O-ring, with a test area of  $0.22 \text{ cm}^2$  and compression area of  $0.097 \text{ cm}^2$ , however 80 % of the trials resulted in breakthroughs from the compressed area. These results indicate that areas of the GDL that are compressed are preferential pathways for liquid water transport. These results are counter-intuitive because, in general, the compression of hydrophobic porous media results in smaller mean pore sizes. In the absence of other effects, a decrease in hydrophobic pore size results in a marked decrease in liquid permeability [128]. Thus, it would be expected that liquid water transport through an uncompressed GDL would be favored over an otherwise similar locally compressed GDL, whereas the opposite is observed here.

It should also be noted that the tendency for liquid water to breakthrough the compressed regions of the GDL cannot be attributed to the potential decrease in thickness associated with this compression. As shown in Fig. 3.3 and Fig. 3.4, liquid water appeared near the surface of the GDL under the uncompressed region first (Path 1); however the preferential pathway for water transport leading to breakthrough occurred several seconds later (Path 2) under the compressed region. The tendency for breakthrough to occur through the thinner region of the media does not hold since the first pathway for liquid percolation appeared under the uncompressed region, which would theoretically be the thicker region. In general, the thickness of the material only influences the pressure drop due to viscous dominated flow, and in the systems considered here, the pressure drop is dominated by capillary forces, rather than viscous forces. Furthermore, the influence of the material thickness only takes effect at the point of breakthrough. Prior to breakthrough, the boundary condition just beyond the advancing liquid/gas interface is atmospheric pressure throughout the media. In summary, the filling phenomena is dominated by capillary forces, and a thinner material would only result in earlier breakthrough if it had pores of equivalent

or larger size than the thicker regions. However, in contrast, a general decrease in the mean pore size in the through-plane of the GDL is expected under compression.

These results presented here suggest that the compression of the GDL resulted in additional effects that significantly influence liquid water transport in these materials. The effect of compression on the GDL morphology is investigated next.

### Compression Effects on GDL Microstructure

Using the Hitachi S-3500N SEM as a conventional high-vacuum SEM, the morphological changes in the microstructure of the GDL after compression were investigated at varying pressures. Fig. 3.6 (a) shows an SEM image of a Toray TGP-H-060 GDL at 200x magnification prior to compression, with a hand-held 1 cm x 1 cm sample (inset). This image illustrates that without compression the GDL fibers are intact. Fig. 3.6 (b) shows the intact PTFE coating on the uncompressed GDL at 800x magnification, which is further enlarged to 4,000x magnification in (c). Fig. 3.6 (b) and (c) show that the PTFE coating tends to accumulate on the webbing of carbonized thermoset resin, which binds the carbon fibers together. Despite the localized tendency for PTFE to accumulate in the areas where fibers intersect, the PTFE treatment of the entire GDL surface is generally continuous.

To investigate how compression affects the morphology of the GDL, the SEM was used to visualize GDL samples ( $0.25 \text{ cm}^2$ ) that were compressed at 0.18 MPa, 0.36 MPa, 0.68 MPa, and 1.37 MPa for five minutes. At 1000x magnification, Fig. 3.7 shows the breakage in the PTFE coating. Fig. 3.7 indicates that the breakage occurs in the “webbing”, but that also PTFE can detach from the fibers, as shown in the upper left carbon fiber. This image also shows some PTFE coating that has been twisted and pulled midway through the left image.

Fig. 3.8 shows the SEM images of the GDL at 200x magnification after it was compressed for 5 minutes at (a) 0.18 MPa, (b) 0.36 MPa, (c) 0.68 MPa, and (d) 1.37

MPa. These images show that as the compression pressure increased, the severity and extent of the damage also increased. With a compression of 0.18 MPa, the damage to the GDL was nonuniform. This nonuniformity was attributed to the surface roughness of the GDL. As the GDL is compressed, the thickest areas of the GDL will experience damage first. However, as the compression pressure increased, the damage became more isotropic throughout the sample. The damage observed in the sample compressed at 1.37 MPa in Fig. 3.8 (d) was characteristic of the damage to the GDLs used in the fluorescence microscopy visualizations, since they were clamped at 1.5 MPa, which is characteristic of reported pressures encountered in fuel cell studies [70, 75].

The irreversible damage at the surface of the GDL had a dramatic impact on water transport behaviour, particularly at the breakthrough location. As the fibers break and PTFE coating disintegrates, the fiber edges that were not treated with PTFE become exposed, locally producing a greater proportion of hydrophilic to hydrophobic surface areas. According to the sessile drop method [131], the contact angle of Toray TGP-H-060 with 9 wt. % is  $156^\circ$ , which is expected to be approximately the contact angle for the GDL used in this work (TGPH-060 with 10 wt. %). In contrast to the hydrophobic PTFE coated fibers, the contact angle of an untreated carbon fiber is likely to be similar to an untreated graphite plate that has a contact angle of  $70\text{--}80^\circ$  [38]. The multiphase flow in the GDL would also become more complex due to the mobile PTFE components that were damaged. These detached chips of PTFE would presumably be removed from the GDL with the bulk water transport. This would, overall, reduce the hydrophobicity of the GDL compared to the original material. The exposure of untreated carbon fiber surfaces combined with the detachment of treated binder and fiber are expected to result in changes to the surface properties of the GDL. Untreated fiber surface areas have a lower adhesion energy to the non-wetting phase (liquid water) compared to treated surfaces, and the detachment of treated material also results in a localized decrease in surface adhesion energy resulting in

a lower contact angle. Together, this results in localized hydrophilic surface areas, which provide preferential pathways for water transport in the bulk hydrophobic GDL. Larger pores at the surface of the GDL may have also been created by fiber breakage, which would have provided a decrease in flow resistance in these hydrophobic regions. Pekula et al. [28] attributed their observations of the tendency for water to accumulate along channel walls and under the land area to slower gas velocities; however the work presented here suggests that the areas where the GDL is compressed become preferential pathways for liquid water transport.

## 3.2 Concluding Remarks

Compressing a PEMFC GDL has a large influence on liquid water transport behaviour as well as on the GDL microstructure morphology. Fluorescence microscopy was applied to provide *ex situ* visualizations, showing that the compressed GDL provides preferential pathways for water transport and breakthrough. SEM images clearly illustrating the degradation of the GDL under varying compression pressures were presented. The irreversible damage at the surface of the GDL consisted of fiber and PTFE coating breakage and deformation, which locally produced greater proportions of hydrophilic to hydrophobic surface areas. Preferential pathways for water transport were a result of these localized hydrophilic pathways in the bulk hydrophobic GDL. The present work shows that compression alters liquid water transport and favors flow in the compressed areas of the GDL (under the land area) due to both morphological changes and possible loss of hydrophobicity. With respect to fuel cell operation, this liquid water transport behaviour may be beneficial as water can be channeled to where transport is less critical. Liquid water transport in the fuel cell could be further controlled by pre-compressing the material in strategic locations to facilitate removal of excess water in an assembled cell.

Table 3.1: Liquid Breakthrough Pressures

Trial #	Breakthrough Pressure (kPa)
1	4.8
2	5.6
3	5.0
4	5.1
5	5.7
6	5.8
7	5.7
8	5.7
9	5.7
10	5.7

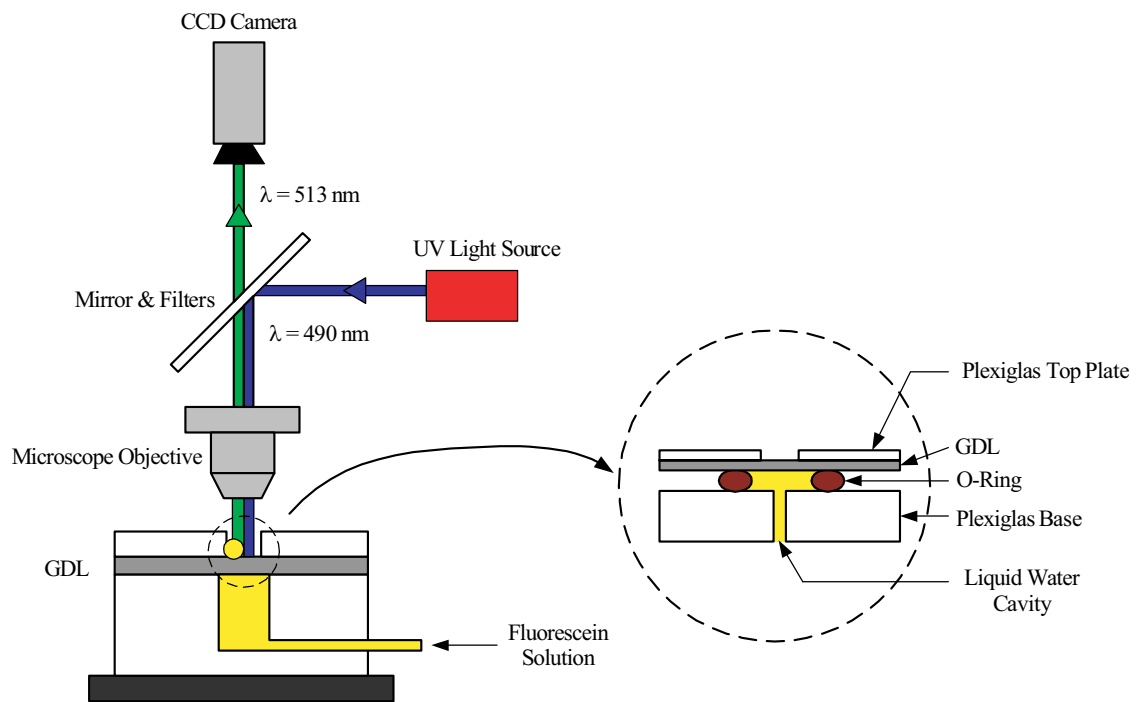


Figure 3.1: Schematic of the fluorescence microscopy and GDL clamping apparatus.

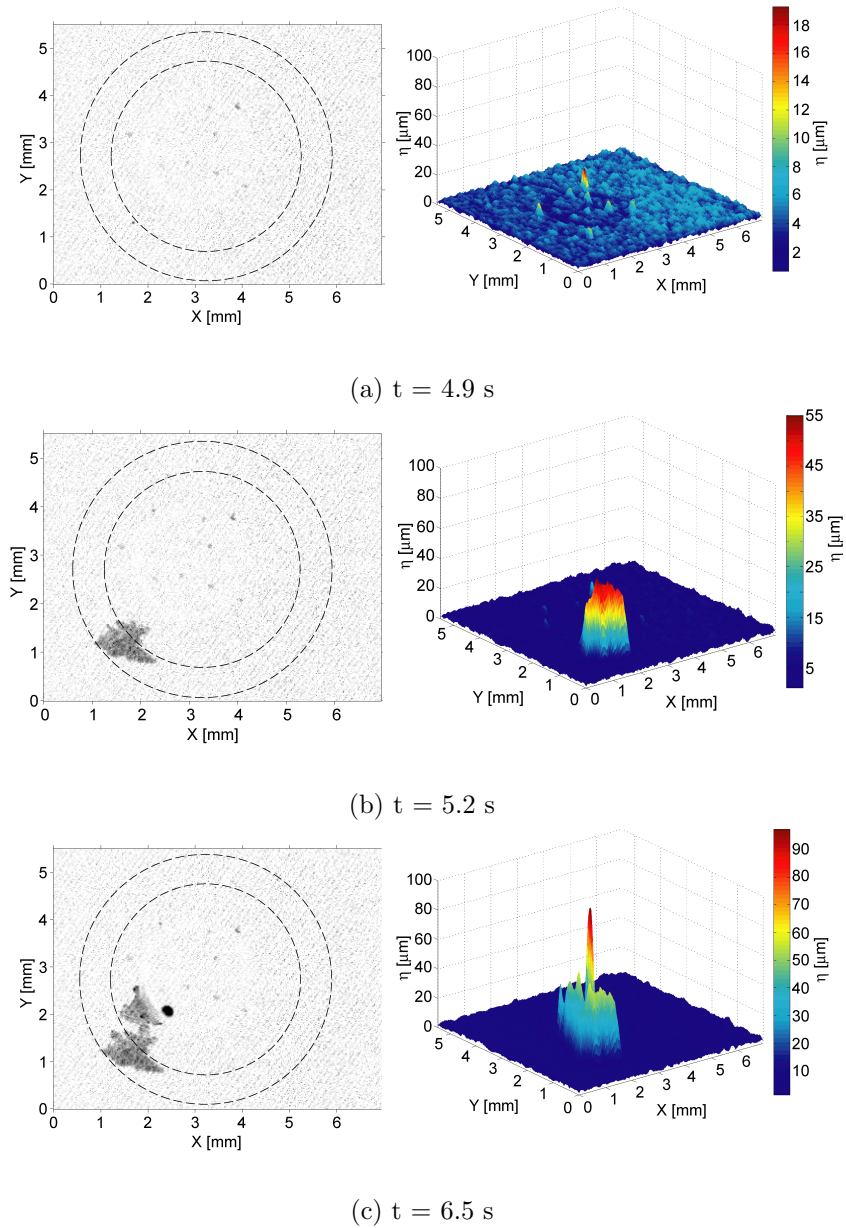


Figure 3.2: Digital images from fluorescence microscopy showing the evolution of water transport at (a)  $t = 4.9$  s, (b)  $t = 5.2$  s, and (c)  $t = 6.5$  s. Images to the left have been inverted for clarity, with the areas compressed by the O-ring shown as the area between the concentric dashed circles. To the right of each image is the three-dimensional rendering of the signal intensity.

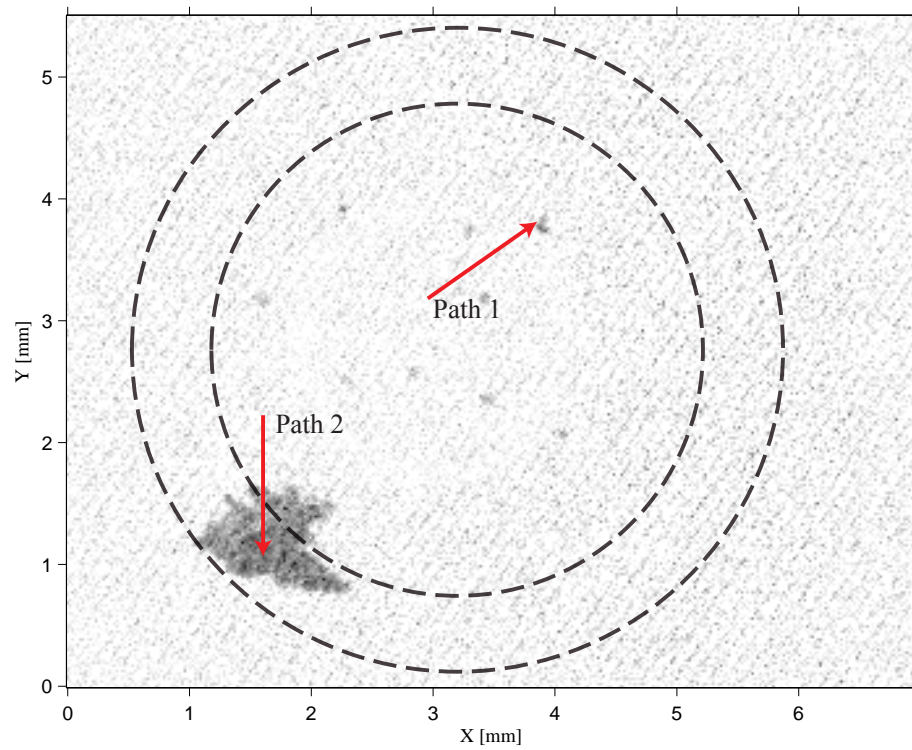


Figure 3.3: Inverted fluorescence image at 5.2 s showing flow paths 1 and 2 shown in Fig. (3.4). The areas of the GDL that are compressed exist between the concentric dashed circles.

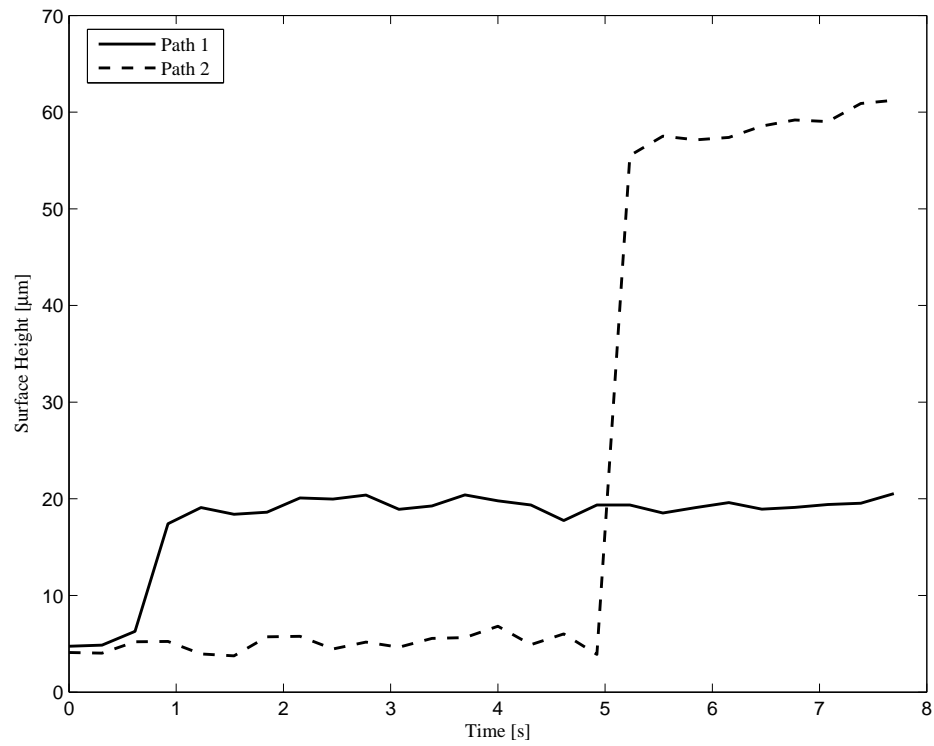


Figure 3.4: The liquid water surface height determined via correlation with fluorescence intensity of Path 1 and 2, where Path 1 appears in the uncompressed GDL and Path 2 appears in the compressed GDL.

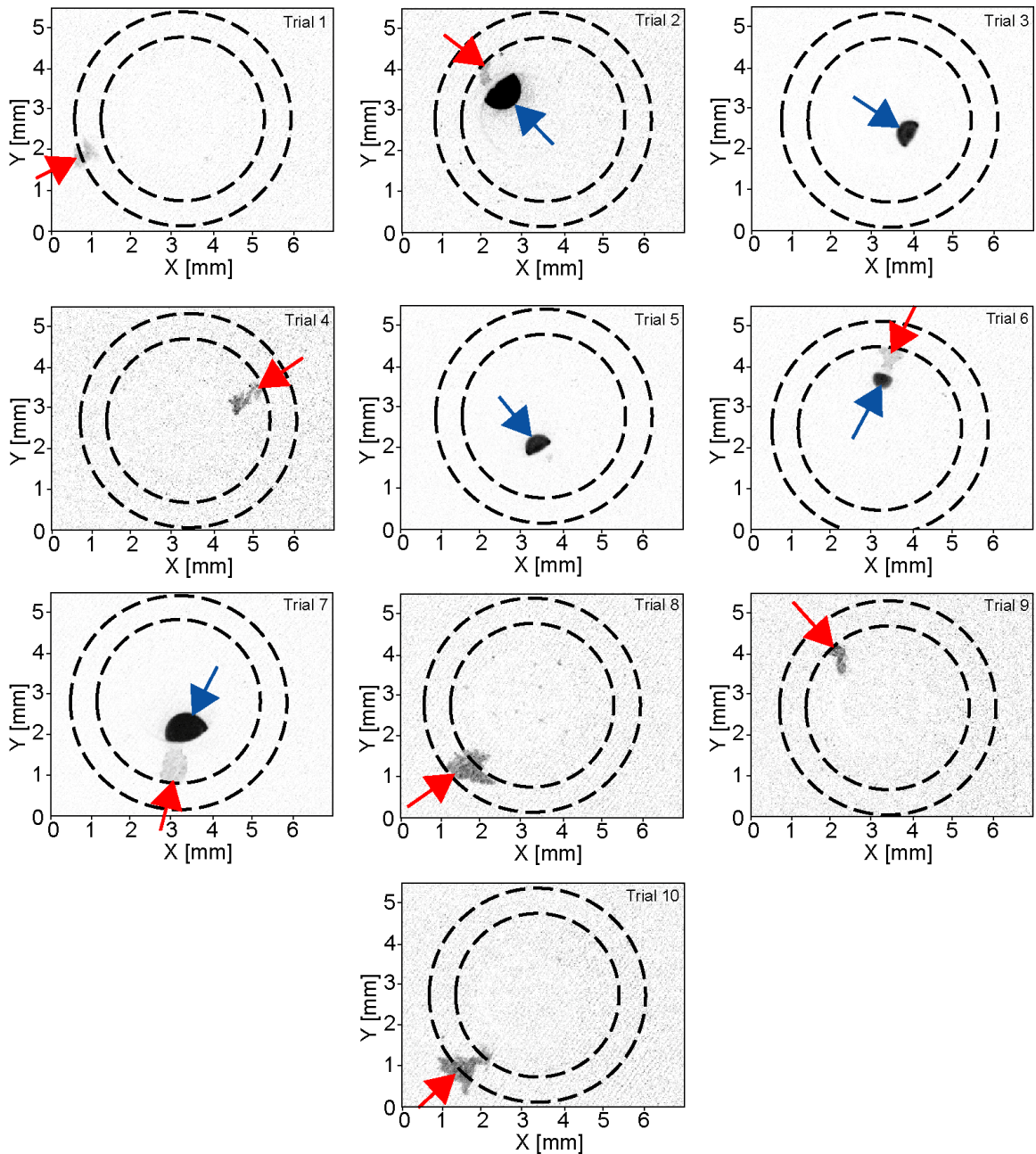


Figure 3.5: Inverted fluorescence images showing the liquid water breakthrough location with respect to the compression O-ring, where all trials except for Trial 3 and Trial 5 resulted in breakthrough originating in the area above the compression O-ring. Red arrows indicate where breakthrough coincided with the compression region. The blue arrows indicate where excess fluid exited through the outlet hole, post-breakthrough.

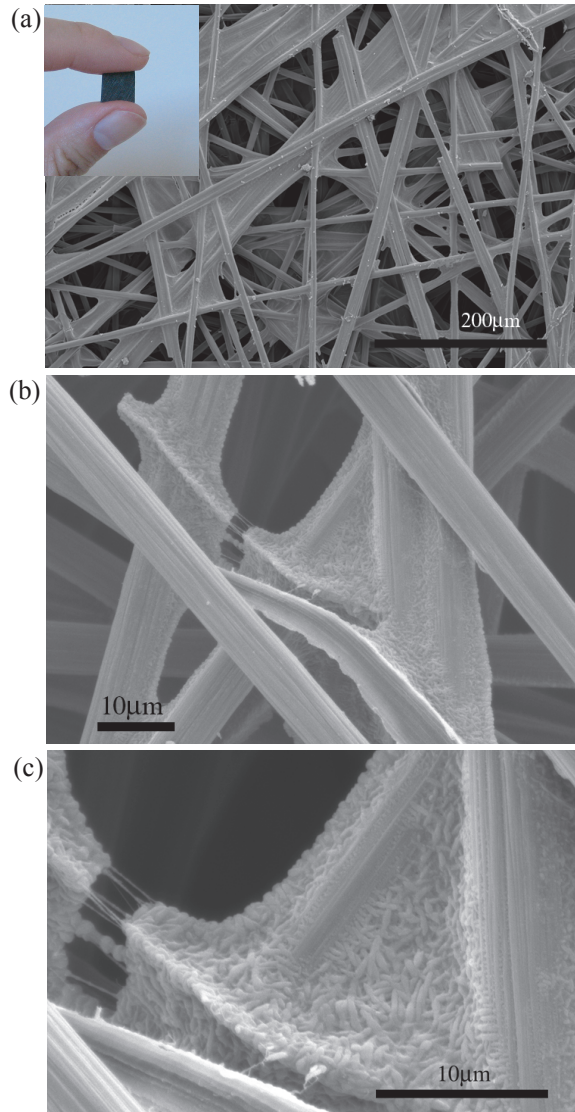


Figure 3.6: SEM images of a Toray TGP-H-060 GDL with 10 wt. % PTFE treatment before compression at (a) 200x magnification with a hand-held 1 cm x 1 cm sample (inset), (b) 800x magnification, and (c) enlarged image of (b) at 4,000x magnification.

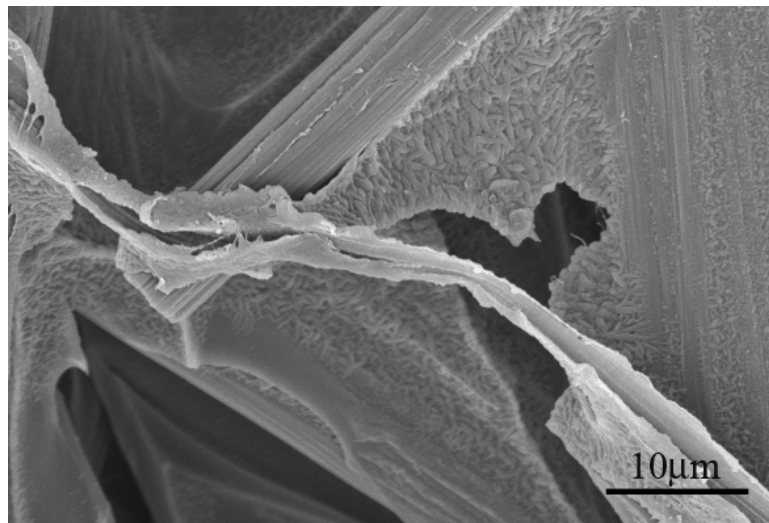


Figure 3.7: SEM image of a Toray TGP-H-060 GDL with 10 wt. % PTFE treatment after it was compressed for five minutes at 0.18 MPa at 1000x magnification showing the damaged PTFE coating.

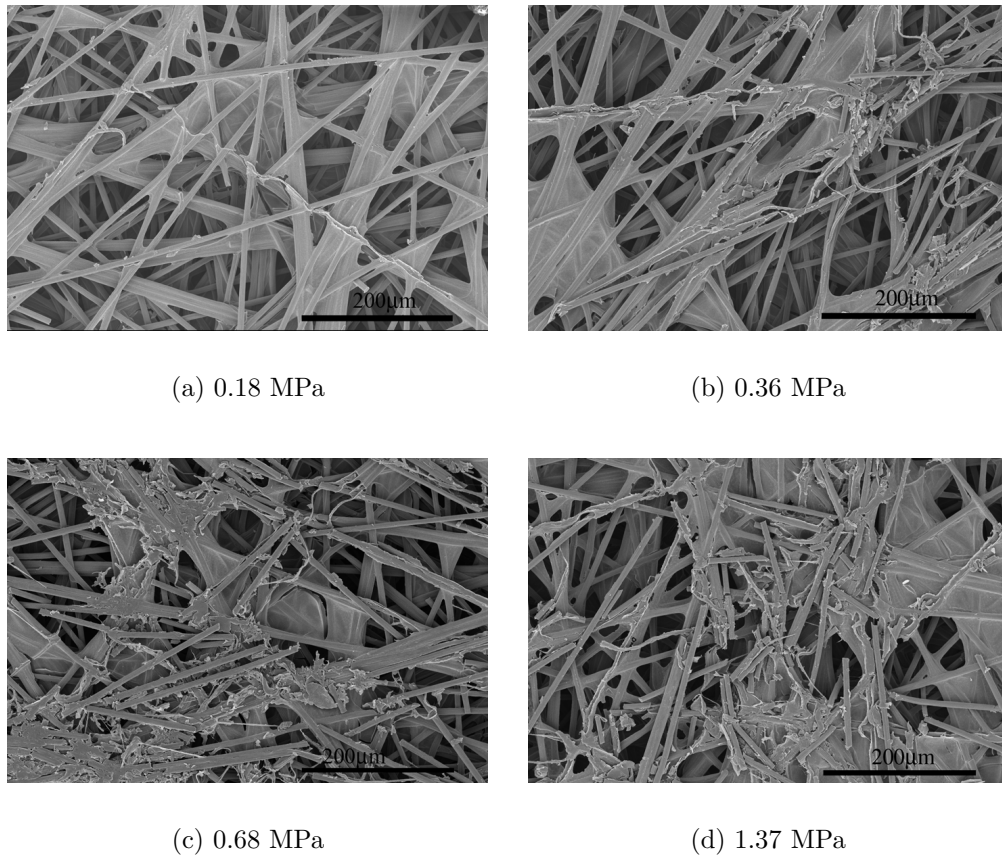


Figure 3.8: SEM images of Toray TGP-H-060 GDLs at 200x magnification after five minutes of compression at (a) 0.18 MPa, (b) 0.36 MPa, (c) 0.68 MPa, and (d) 1.37 MPa. Each image shows a different GDL sample.

## Chapter 4

# Dynamic Liquid Water Transport

Although liquid water transport in a cathode gas channel has been studied [39,41,43], little has been done to investigate the associated microscale transport phenomena. In this chapter, the dynamic behaviour of liquid water transport in a simulated gas flow channel is presented. Specifically, the emergence and detachment of droplets are of interest, and the use of fluorescence microscopy enables the observation of this phenomena at the microscale.

### 4.1 Apparatus

Figure 4.1 shows the experimental apparatus which consisted of the gas flow channel apparatus on the fluorescence microscope stage and a schematic of the gas flow channel apparatus in cross-section. The GDL was placed between a Plexiglas base and a PDMS channel structure with dimensions (3.7 mm x 4.5 mm). The relatively large channel dimensions were chosen such that droplet emergence and transport could be studied in the absence of sidewall effects. A silicone rubber gasket was placed between the GDL and Plexiglas base to prevent leakage.

Air was delivered to the gas channel and controlled with a rotameter (Omega

FL-3840G). Liquid water was injected through the bottom surface of the GDL using a syringe pump (Harvard Apparatus PHD 22/2000) connected to the Plexiglas base with Teflon FEP tubing (Upchurch Scientific, WA). Unless otherwise stated, liquid was delivered at a rate of 0.005 mL/min. Assuming no net water transport between anode and cathode in a PEMFC, this water flow rate would correspond to high current density operation<sup>1</sup> [41]. The liquid pressure was measured with a pressure transducer (Omega PX4202-005G5V) with an operating range of 0-34 kPa. This pressure transducer was placed close to the Plexiglas base inlet. The pressure transducer was connected to a DAQ system (National Instruments, Austin, TX ). The channel structure was cut from a PDMS layer. With a contact angle of 78°, the PDMS channel is an appropriate material to simulate graphite bipolar plates with a contact angle of roughly 70-80° [38]. A Plexiglas top plate was clamped above with eight screws with a torque of 1 in·lb/screw. An upright fluorescence microscope was used to capture the through-plane evolution of liquid water transport. To facilitate fluorescence imaging, fluorescein dye was used to tag the liquid phase (0.1 mM). The low dye concentration was used to ensure the physical properties of the solution effectively matched those of pure water [130]. Images were captured using a charge-coupled device (CCD) camera (Orca-AG, 12 bit) with a frame rate of 9.3 frames/s and binning of 4 x 4, resulting in a resolution of 325 x 257 pixels. Unless otherwise stated, all fluorescence images were obtained with a 5x magnification objective with a numerical aperture,  $NA = 0.12$ , and a spatial resolution of 8.14  $\mu\text{m}/\text{pixel}$ . Top view fluorescent images captured the evolution of liquid transport in the top few layers of the GDL, where the depth of optical access was limited by the opaque nature of the material.

In the work presented here, liquid water was introduced from one side of the GDL

---

<sup>1</sup>Schulz et al. [132] argue that flow rates of this order correspond to unrealistically high current densities; however, this is not the case when considering the likelihood of discretely distributed sites of liquid water formation in a fuel cell. Under this consideration, the corresponding surface area with which a given water injection rate is associated would be larger than the masked water inlet area used in these *ex-situ* experiments. Therefore, the liquid injection rates employed here are considered reasonable for the consideration of high current densities.

from a single localized source. The conditions imposed here, albeit simplified, provided insight into an operating fuel cell when considering the likelihood of distributed sites of liquid water formation in the cathode. Furthermore, with continuous liquid water formation in the catalyst layer or the lower layers of the GDL, liquid water will percolate through discrete locations of the GDL due to its porous and hydrophobic nature. However, these experiments did not capture the thermal gradients present in fuel cells, and the occurrence of condensation in the GDL may affect the behaviour of water transport observed in these experiments.

## 4.2 Results & Discussion

### 4.2.1 Droplet Growth

Fig. 4.2 shows the liquid water pressure measured as a function of time when water was injected at a constant rate of 0.005 mL/min with an average air flow velocity of 2 m/s. After 20 minutes of liquid injection, the system reached a critical pressure, herein termed the *breakthrough pressure*, at which droplets began to appear on the surface of the GDL. The breakthrough pressure refers to the liquid water pressure required to penetrate the through-plane of an initially dry GDL. The initial breakthrough refers to the moment at which the first droplet appears on the surface of an initially dry GDL. In the pre-breakthrough period, the linearity of the pressure increase over time was mostly due to the expansion of the fluid delivery system. Post-breakthrough, individual droplets, which correspond to the pressure peaks, emerged and detached for the following 30 min. However, after 50 min, the gas channel became populated with water slugs, and individual droplets no longer appeared. This experiment was characteristic of several repeated trials, such that the initial breakthrough of liquid water in the GDL was preceded by a substantial growth of liquid water pressure, and breakthrough occurred when a critical pressure was reached.

The growth of individual droplets over time was tracked through image analysis. Fig. 4.2 (b) shows the droplet diameter versus time for three individual droplets that emerged at the following three times:  $t_{i1} = 24:07$  min,  $t_{i2} = 33:32$  min, and  $t_{i3} = 53:55$  min (also marked in Fig. 4.2 (a)). All three droplets grew to approximately 2.4 mm in diameter before detaching from the GDL surface; however as time proceeded, the droplet took longer to grow to that critical size. Fig. 4.2 (b) (inset) shows a series of raw fluorescence images used to track the growth of the droplet for  $t_{i1} = 24:07$  min. The dark portion of the images correspond to the GDL, and the bright white areas correspond to the liquid water. This figure shows that in the absence of pinning, the droplet reached a critical size before detachment at a given air flow velocity. However, the growth period required for the droplet to reach that size depended on the amount of time that had passed since the initial breakthrough. When there was more liquid water pressure in the system, as there was at time 24:07 min, the droplet grew much more quickly than at later times when the pressure had significantly decreased.

In a typical fuel cell with channel geometry 0.5 mm x 0.5 mm, liquid droplets will clearly not reach the critical size observed here. However, these results indicate that droplets would also reach a critical size (albeit smaller) before detachment and experience similar pinning, with the same GDL material.

## 4.2.2 Droplet Pinning

In all the experiments, individual droplets emerged, grew, and detached from the GDL. However, it was commonly observed that over time these droplets left residual liquid water particles on the GDL, which provided pinning sites for other droplets. Droplets became pinned to the GDL due to its high surface roughness and high contact angle hysteresis. Under the same circumstances with a perfectly smooth and hydrophobic surface, a droplet might easily detach and roll away from the breakthrough location. However, the GDL surface was composed of randomly oriented carbon fibers

with non-isotropic wettability. Droplets situated on this highly rough surface experienced fewer tendencies for detachment due to longer contact lines between the droplet and fibers and due to contact angle hysteresis. Furthermore, residual water particles may have also increased the tendency for droplet pinning. Typically, a transition occurred between individual droplet formation and detachment to slug formation, as shown in Fig. 4.2 (a). Individual droplets became pinned in the vicinity of the breakthrough location. After subsequent droplets emerged and coalesced with the pinned droplet, the droplet detached after reaching a critical size. Pinning affected droplet emergence frequency and size because before the droplet reached its critical radius for departure, the droplet commonly coalesced with the pinned droplet. Fig. 4.3 (a) is a raw image (top view) obtained from fluorescence microscopy showing a GDL pore (white) that was saturated with liquid at  $t = 34:01$  min, and Fig. 4.3 (b) is a raw image showing a spherical droplet sitting on top of that saturated pore that connected the droplet at  $t = 34:03$  min. Due to the air flow from right to left, the droplet shifted to the left. The contact line between the droplet and the GDL pore can be seen in Fig. 4.3 (a), since this contact line was defined by the saturated pore size. In contrast, after several cycles of droplet detachment, Fig. 4.3 (c) shows a pinned droplet at  $t = 1$  h 39 min. The wetting contact line between the droplet and the GDL was no longer defined by the droplet's originating pore. Droplets emerged from a location directly to the right of the pinned droplet. These droplets detached at a much smaller critical size than described in Fig. 4.2. Once detached, these droplets immediately coalesced with the pinned droplet, contributing to an increasingly larger droplet. Although the GDL surface was hydrophobic and air flow velocities initially provided sufficient force to detach droplets, over time the GDL surface became prone to droplet pinning and eventual slug formation.

### 4.2.3 Dynamic Breakthrough Locations

It has been found that water emerged from the surface of the GDL in preferential locations corresponding to the path of least resistance [8]. Here, the determination of preferential water breakthrough locations was observed to be a dynamic process, i.e. the location of breakthrough changed over time. Observations suggest that new breakthrough locations arose due to a rearrangement of water pathways within the GDL. As a droplet was removed by air flow in the gas flow channel, the liquid pressure within the GDL continued to grow. During this pressure increase, it is conjectured that the interconnection of water pathways within the GDL evolved such that the preferential pathway for breakthrough may have changed. This rearrangement, typically accompanied by a pressure increase, was followed by a drop in pressure associated with a quick succession of droplets. Such behaviour is consistent with the *ex situ* observations of Litster et al. [45] and the recent *in situ* measurements of Manke et al. [36], who termed the phenomenon as *eruptive transport*. This eruptive transport can be explained by the pressure increase measured in this work. It was observed that when a new breakthrough location formed, the old breakthrough location receded (shown in Fig. 4.4), which suggests the extent of branching within the GDL. Fig. 4.4 shows the time evolution of changing breakthrough locations over a period of approximately 2 min. The first frame ( $t = 0$  s) shows the droplet that emerged from a preferential breakthrough location, and at the same time a droplet emerged from a new breakthrough location (lower right). As several droplets emerged and departed from the new location, the droplet sitting at the top of the viewing area receded until only traces were visible at  $t = 114$  s. Although channeling has been recently proposed to be the dominant mechanism of water transport in the GDL [45], these new results suggest that it is a combination of channeling with the growth of an interconnected dynamic network of water pathways within the GDL that may dominate the mechanism of water transport.

#### 4.2.4 Volume of Fluid Simulations

To better understand and highlight the driving mechanisms, idealized Computational Fluid Dynamics (CFD) modelling was performed with the Volume Of Fluid (VOF) method using the commercial CFD package, FLUENT 6.2.16. The VOF method, developed by Hirt and Nichols [133] is a popular method of solving time-dependent flows by applying a surface-tracking technique (see Zhu et al. [134] for more details). Fig. 4.5 (a) illustrates the two-dimensional computational domain, which consisted of a  $375 \mu\text{m} \times 100 \mu\text{m}$  gas flow channel. The air inlet is at the left boundary, and the two phase outlet is at the right boundary. Two microchannels, A and C ( $25 \mu\text{m} \times 100 \mu\text{m}$  and  $50 \mu\text{m} \times 100 \mu\text{m}$ , respectively), are connected by a  $25 \mu\text{m} \times 200 \mu\text{m}$  horizontal channel (B). Channels A and C are connected to the gas flow channel. A structured orthogonal computational mesh consisting of 2,164 cells was used. The adequacy of this grid was tested by increasing the number of grid nodes by 100 %, and similar transport processes were obtained. Simulations were performed with time steps of  $10^{-7}$  s. A no-slip boundary condition was imposed along the walls of the domain. A contact angle of  $70^\circ$  was set for the top wall, and  $140^\circ$  for the bottom wall and the microchannels that simulate GDL pores. The air flow velocity was set to 10 m/s at 100 kPa, and liquid water was injected at a velocity of 0.1 m/s. Fig. 4.5 (b) shows the time evolution of channel filling connected to a gas channel. At  $t = 0.0010$  s, both  $25 \mu\text{m}$  channels (A and B) fill simultaneously. However, when channel A becomes completely filled, the capillary force required to form a droplet exceeds the threshold capillary force required for the pathway in channel B to continue filling the horizontal channel. Thus, channel B continues to fill with liquid water. Once the pathway in channel B reaches the larger pore (C), liquid water flows into channel C while flowing out of channel A. The liquid height in channel A recedes, and the larger channel (C) provides the breakthrough location for the first droplet. The time evolution of water transport between two competing channels shows that in the presence of an interconnected pathway of water channels, dominating preferential pathways can lead

to the recession of initial pathways. The observations described in Fig. 4.4 supported by these CFD VOF simulations shown in Fig. 4.5 help explain the observed dynamic fingering and *eruptive transport* mechanisms in the literature [36, 45].

### 4.3 Concluding Remarks

The dynamics of liquid water transport through and on the surface of a GDL was investigated with a simulated gas flow channel. Liquid water was injected through the bottom surface of the GDL, and the through plane liquid pressure drop, droplet emergence and droplet detachment were studied. The dynamic behaviour of water transport was observed with the use of fluorescence microscopy, and the through-plane liquid pressure drop was measured with a pressure transducer. With an initially dry GDL, the initial breakthrough of liquid water in the GDL was preceded by a substantial growth of liquid water pressure. Post-breakthrough, droplets emerged with high frequency, until a quasi-equilibrium liquid water pressure was achieved. The droplet emergence/detachment regime was followed by a transition into a slug formation regime. With an initially dry GDL, a pore that defined the contact line between a spherical droplet and the GDL surface was typically quite small. After the GDL surface had been exposed to droplet particles, the surface became prone to droplet pinning and flooding. Droplets became pinned to the GDL's rough surface with large wetting contact lines, and much higher air flow rates were needed to remove these pinned droplets. The changing breakthrough location suggested a dynamic and interconnected network of water pathways within the GDL, which was supported by numerical results from an idealized test system simulating the filling behaviour of liquid water within two competing pathways. These simulations showed that once a new preferential pathway was found, less preferable pathways receded. These results supported the experimental observations of receding droplets. The work presented in this chapter provided insight into the changing behaviour of liquid water transport

in the GDL when operating under nominally static conditions.

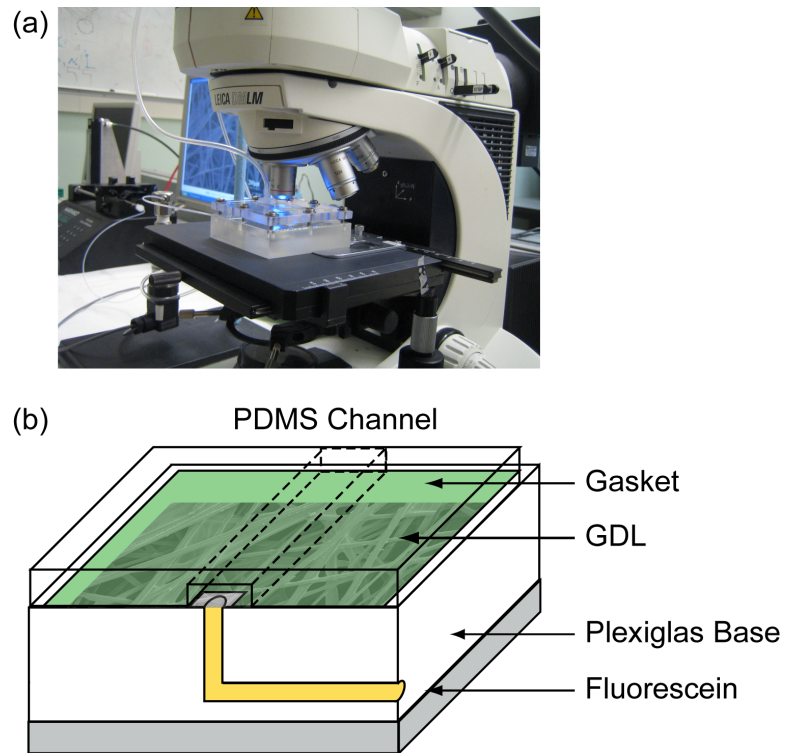


Figure 4.1: Simulated gas flow channel apparatus: (a) photograph of the gas flow channel apparatus on fluorescence microscope stage, and (b) schematic showing the apparatus cross-section.

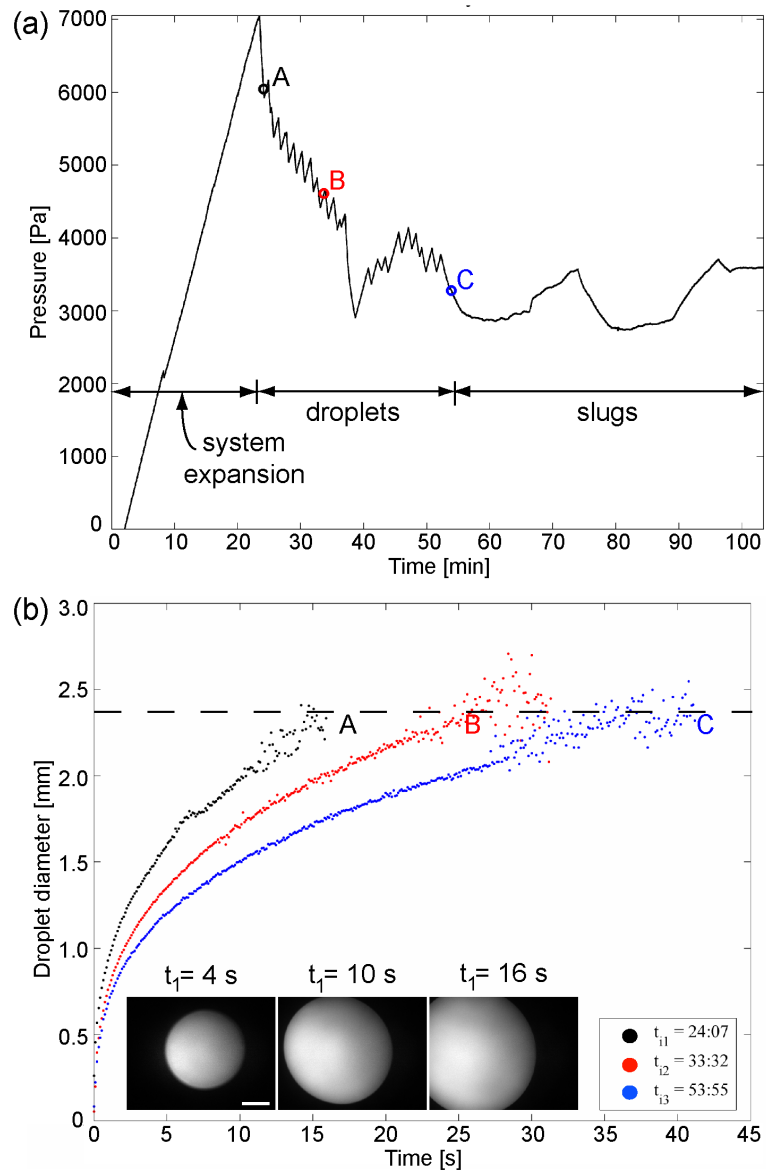


Figure 4.2: Dynamic water transport behaviour through an initially dry GDL: (a) liquid water pressure showing the time periods in which single droplets emerged and detached from the GDL surface and in which slug formation led to channel flooding, and (b) tracking the growth of three different droplets (A, B, and C, which correspond to times shown in (a)) ( $t=0$  corresponds to incipient droplet formation). Raw fluorescence images are shown inset for the  $t_{i1}$  case at times indicated. Length bar indicates 0.5 mm.

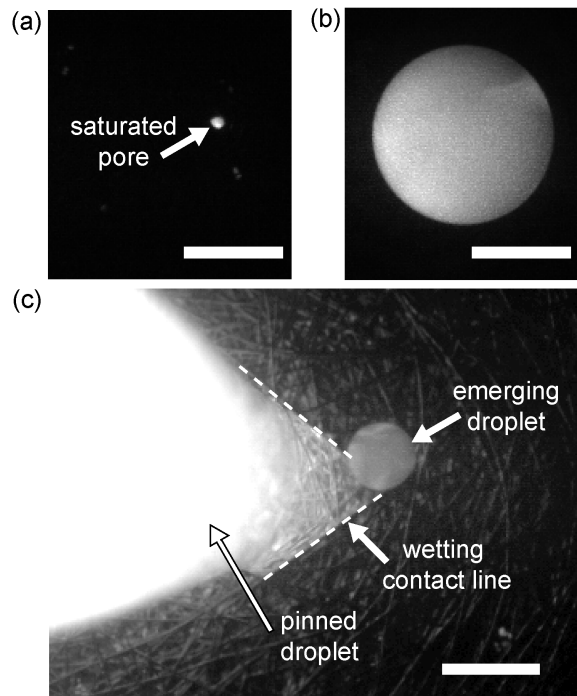


Figure 4.3: Top view raw fluorescence images (white areas indicate location of liquid water) captured with a 2 m/s air flow velocity at (a)  $t = 33:01$  min showing the saturated pore immediately prior to droplet emergence, (b)  $t = 33:03$  min showing a droplet sitting above the saturated pore, and (c) after several droplet emergence/departure cycles showing a large droplet pinned to the GDL surface to the left of an emerging droplet. The air flow direction is from right to left, and the length bars are 0.5 mm long.

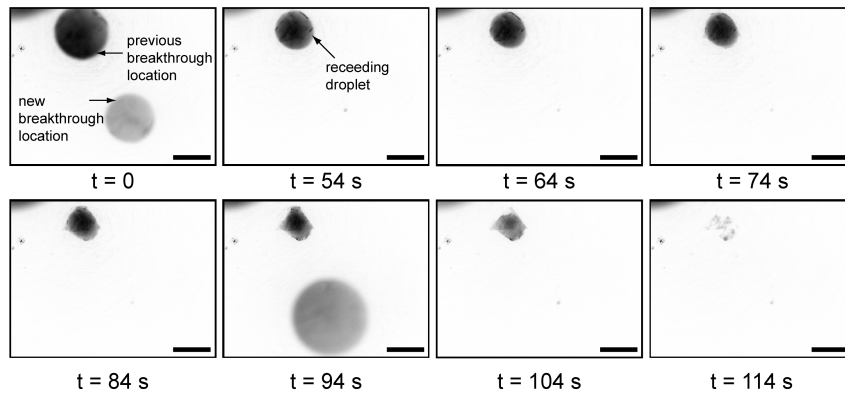


Figure 4.4: Time series of fluorescence images showing the recession of a droplet formed above the previous breakthrough location. A new breakthrough location has emerged in the lower right hand corner of field of view. The images have been inverted for clarity, and length bars represent 0.5 mm.

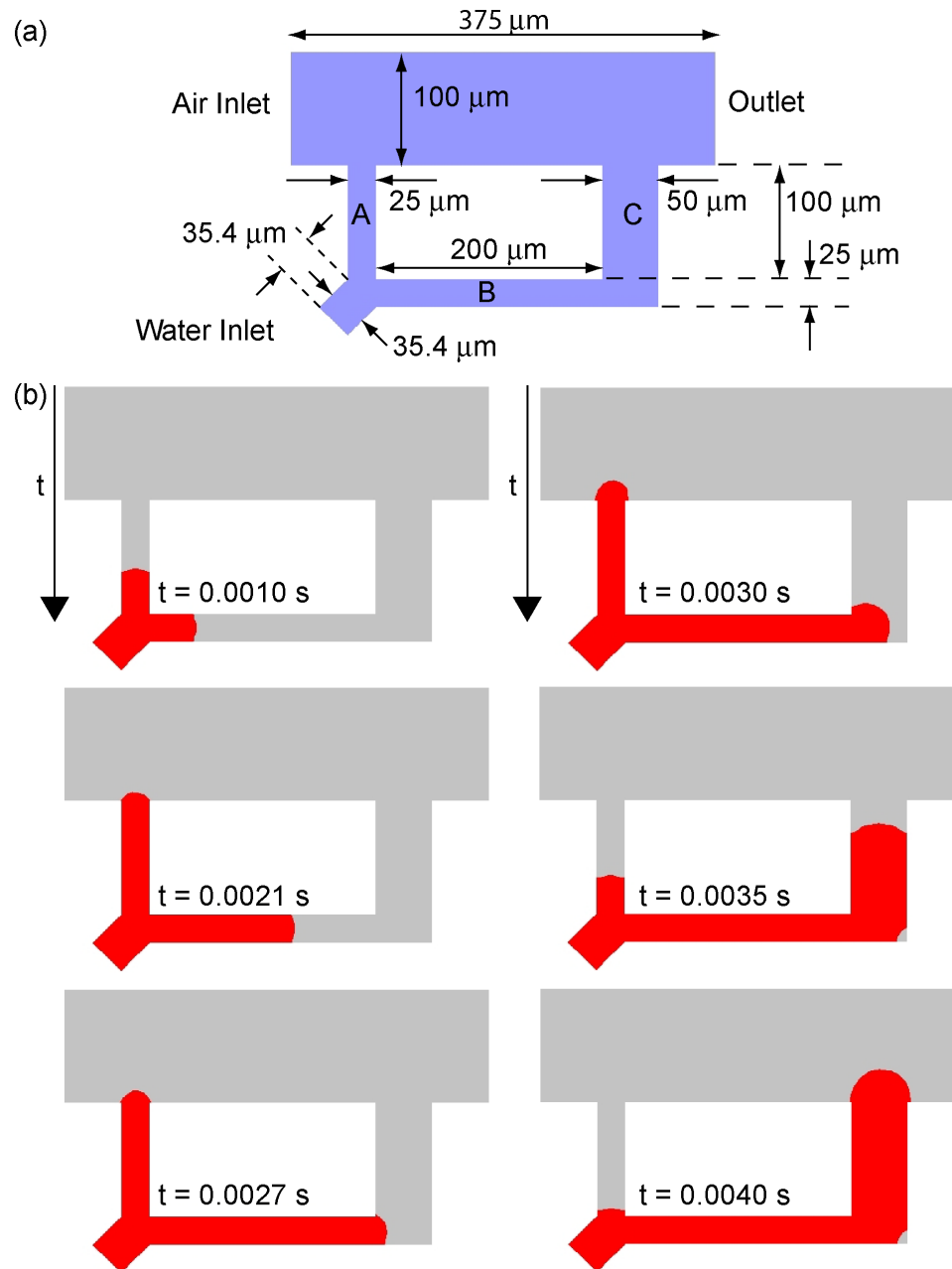


Figure 4.5: Volume of fluid (VOF) simulation results: (a) schematic showing the computational domain of the gas flow channel with two GDL pores (channels A and C), and (b) time series of VOF simulation results showing the primary filling of the smaller channel (A) followed by the secondary filling of the larger channel (C). (Red represents liquid water, and gray represents air.)

## Chapter 5

# Pore Network Designs for Directed Transport

Work to date in the area of pore network and experimental modelling of porous media has focused on characterizing existing media. In this chapter, the network model presented in [122] is utilized together with experimental microfluidic networks [115] to investigate pore networks designs that allow controlled water transport in the GDL, with a focus on the breakthrough liquid water pattern and overall network saturation. In keeping with the random nature of GDL materials, all pore networks studied here are generated with a random distribution of throat widths. Longer range geometrical variations (biasing) added to these networks are of interest in comparing the influence on water transport. This is the first application combining numerical modelling and experimental microfluidic networks to investigate how the microstructure of the GDL could be engineered to direct and control water transport.

## 5.1 Methodology

Pore network modelling provided a method to evaluate the liquid water transport through the GDL in a PEMFC, as indicated in Fig. 5.1. In this work, pore networks with pore size characteristics of the GDL [131] were designed with a software package developed in-house, and the invasion percolation with trapping algorithm (adapted from that originally developed by Markicevic et al. [122]) was used to evaluate the drainage process. Once a photomask design was chosen, the photomask was generated and printed with a high resolution printer. The photomask was employed during the photolithographic microfabrication process (performed by V. Berejnov), where a microfluidic pore network was generated. The spread of water into the microfluidic network was monitored using fluorescence microscopy, and flow patterns associated with the time series evolution of liquid water transport through the network were recorded. The pore network design process is illustrated in Fig. 5.2. The experimental breakthrough patterns were then compared to pore network simulations based on Wilkinson and Willemsen’s algorithm for invasion percolation with trapping [95,122].

### 5.1.1 Pore Network Modelling

The invasion percolation algorithm with trapping [95] was used to investigate deterministic realizations of pore network filling. The two-dimensional model accounts for capillary dominated drainage and cluster formation in a regular square capillary network of size  $n_L \times n_L$  pores. The porous media is represented by a matrix of pores and connecting throats. The invading phase (water) enters the network along the top side (inlet), and advances through the network in a series of quasi-static steps by occupying available throats having the largest throat radius. The fluid exits through the outlet (opposite side to the entrance), and the invasion process is stopped once breakthrough occurs, where breakthrough is when the first throat at the outlet is filled with the invading fluid. In this work, the deterministic nature of the pore network

invasion process provides a useful feature allowing comparison with experimental results and the evaluation of pore network designs. Fig. 5.1 shows a sample numerical breakthrough pattern in relation to a fuel cell schematic.

### 5.1.2 Microfluidic Pore Networks

Using Matlab 7.0, a pore network was designed, and the coordinates were then imported into Autocad 2007, where the photomasks were drafted. All photomasks were then printed by CAD/Art Services, Inc. (California, USA), with a maximum resolution of 20,000 dpi. The microfabrication process (performed by V. Berejnov) begun with patterning a photoresist resin layer on a silicon substrate. A thin layer of SU8-25 photoresist (25  $\mu\text{m}$  thick) was distributed over the silicone substrate through the use of a spin coater. The photoresist layer was then soft-baked to evaporate solvent and condense the photoresist. The photoresist layer was exposed to a near-UV light source (350 - 400 nm), which allowed for photoresist cross-linkage [135]. The substrates were baked to complete the photoresist cross-linking reaction. Any SU8-25 photoresist substrate that was not exposed to UV light was removed with chemical etching. The pore network was then fabricated by curing a polymer on the patterned template, removing the polymer from the template and sealing the template to a planar surface. Through this rapid prototyping technique, several microfluidic pore networks were generated and tested within a short period of time. A flow diagram summarizing this pore network design and fabrication process is shown in Fig. 5.2. The reader is directed to recent work by Berejnov et al. [115] for specific microfabrication details that are beyond the scope of this thesis.

## 5.2 Pore Network Design

### 5.2.1 Pore Network Structure

A random pore network can be generated in a number of ways. Starting with a blank two-dimensional domain, as shown in Fig. 5.3, square obstacles can be arranged randomly to fill the domain, while overlapping is prohibited. The spaces that are not covered by these square obstacles will constitute the throats and pores. In Fig. 5.3 (a), the network is generated by randomly perturbing a regular lattice of square obstacles. In Fig. 5.3 (b), the domain is filled by adding one square obstacle at a time, until the maximum number of obstacles is reached. Fig. 5.3 (c) shows a randomly arranged network, which is generated by first filling the network with square obstacles (obstacle 1). Once the maximum number of obstacles is placed in the domain, the remaining space is filled as tightly as possible without overlapping with obstacles that are half the size as obstacle 1 (obstacle 2). Again, once the maximum number of obstacles of type 2 are placed, smaller type obstacles can be used to fill the domain. As shown in Fig. 5.3, the benefit of utilizing method (a) is that a higher packing density can be obtained, while maintaining a constant connectivity of four. In method (b), the porosity of the media is very high and difficult to control. In method (c), the obstacle size variation provides a high packing density, but at the cost of varying connectivity and network complexity. All pore networks in this work were generated with the first method (Fig. 5.3 (a)), whereby a regular lattice of square obstacles were randomly perturbed to generate a random network.

### 5.2.2 Randomization

The pore network generation procedure began with a regular lattice of square obstacles. Fig. 5.4 (a) shows a schematic of the regular lattice, where  $w$  is the throat width, and  $L$  is the obstacle square side length. A random translational perturbation

was then applied to each obstacle, where  $\Delta X$  refers to the horizontal translation, and  $\Delta Y$  refers to the vertical translation of the original obstacle. The uniform random distribution of translational perturbations is shown in Fig. 5.4 (c). Fig. 5.4 (d) is the resulting schematic of a portion of the random pore network. The resulting throat width distribution is shown in Fig. 5.4 (e). For a uniform channel height of  $25 \mu\text{m}$ , the hydraulic throat radii distribution is shown in Fig. 5.4 (f). All hydraulic throat radii employed in this work are characteristic of Toray TGP-H-060 GDLs [131].

### Isotropic vs. Diagonal Biasing

To generate an isotropic random pore network, the translation of the regular lattice in the horizontal direction  $\Delta X$  and the vertical direction  $\Delta Y$  must be independent. It is also possible to generate a random pore network with a diagonal bias by coupling the translation of the regular lattice in the horizontal and vertical directions. To implement a diagonal bias of  $\Theta_{bias} = 45^\circ$ , for each square obstacle,  $\Delta Y = \Delta X$ . The ratio of vertical to horizontal obstacle translations can be adjusted to implement the desired diagonal bias for  $0^\circ < \Theta_{bias} < 90^\circ$ , as shown in Eqn. 5.1.

$$\tan \Theta_{bias} = \frac{\Delta Y}{\Delta X} \quad (5.1)$$

### Radial Gradients

The procedure to generate a pore network with a radial gradient is illustrated in Fig. 5.5. The first step is to begin with a regular lattice of square obstacles, as shown in Fig. 5.5 (a). The distance of each square obstacle from the central coordinate axis is labeled  $r$ . The square obstacle is then translated in the radial direction to a new radial distance,  $R$ , from the origin, as shown in Fig. 5.5 (b). The new radial distance,  $R$ , is transformed by the following expression:

$$R = r + \frac{\alpha r^2}{r_{max}} \quad (5.2)$$

Where,  $\alpha$  is the coefficient that is employed to vary the radial gradient of the network. The radial gradient,  $G$ , is the increase in throat width per obstacle, beginning from the central coordinate axis. After a regular network (with radial distance,  $r$ ) is transformed into a new network (with radial distance,  $R$ ), the radial gradient,  $G$ , was numerically measured. Numerical tests yield the following expression between  $G$ ,  $\alpha$ ,  $r_{max}$ , and  $N$ :

$$G = \frac{4r_{max}}{N^2} * \alpha \quad (5.3)$$

Fig. 5.5 (c) shows the resulting pore network design when a radial gradient has been applied to the regular lattice of square obstacles. The final step is to apply a random translation with independent horizontal ( $\Delta X$ ) and vertical ( $\Delta Y$ ) perturbations to each obstacle. An example of the resulting pore network pattern is shown in Fig. 5.5 (d). To quantify the effect of an applied radial gradient on a random network, the radial gradient is normalized with respect to the average throat width of a network without a radial gradient.

The network saturation is calculated to further quantify the effect of liquid transport in a network with a radial gradient. The saturation of the pore network is defined as the number of filled throats divided by the total number of throats in the system, as described in Eqn. 5.4.

$$s = \frac{N_{filled}}{N_{total}} \quad (5.4)$$

### 5.3 Results & Discussion

Numerical and experimental pore networks with identical network designs were invaded with liquid water. Fig. 5.6 shows the numerically and experimentally obtained patterns at breakthrough for 48 x 48 pore networks with (a) isotropic perturbations, (b) diagonally biased perturbations, (c) a radial gradient, and (d) multiple radial gradients. For each network design in Fig. 5.6 shown from left to right are: a scaled down version of the photomask, the numerical breakthrough and the experimental breakthrough patterns. By comparing the percolation patterns shown in Fig. 5.6 (a) and (b), the effect of a diagonal bias on the pore network compared to the isotropically random pore network is evident, even though the difference cannot be detected when comparing their respective photomasks alone. Fig. 5.6 (c) illustrates the effect of a radial gradient on the liquid water transport. With a positive radial gradient, larger throat sizes were located around the outer edges of the pore network. As expected in a hydrophobic medium, the liquid penetrated the throats with the lowest threshold capillary pressure, which were the largest throats. With an applied radial gradient, the liquid saturation was zero at the center of the network and increased with radial distance from the center. With this radial gradient design, liquid water percolated along the outer left and right sides of the network, until breakthrough was achieved. The radial gradient effectively provided directed water transport along the sides of the media.

A larger pore network with several patches with independent radial gradients is shown in Fig. 5.6 (d). The individual patches have been highlighted with gray and black to indicate their size and location. The percolation breakthrough pattern associated with that checkerboard pattern illustrates the preferential pathways created from the application of radial gradients. For all the trials shown in Fig. 5.6, the experimental results agree well with the numerical results, especially when considering that the dynamic effects and contact angle hysteresis that exist in the microfluidic

pore networks were not considered in the model. The agreement between the experimental and numerical results is especially highlighted by the trials shown in Fig. 5.6 (c) and (d), where the percolation pathways leading to breakthrough occurred in the same place.

Of interest from a GDL design perspective is the relationship between the degree of geometric perturbation of the network and its influence on water transport. The dependence of saturation on increasing radial gradient was studied for a 100 x 100 pore network, as shown in Fig. 5.7. Fig. 5.7 shows that as the normalized radial gradient increases, the saturation of the network decreases. This is attributed to the increasing localization and channeling of the invading phase clearly shown by the results. The saturation of individual deterministic simulations is plotted and shown with solid black squares. Since pore network modelling is stochastic by nature, 100 random simulations were performed for each of four points (shown with non-filled black squares), with the average value and standard deviation marked with error bars. The largest standard deviation corresponds to pore networks without a radial gradient, and decreases with increasing radial gradient. With a radial gradient of 0.016/obstacle (i.e. the throat width increases by 1.6 %/obstacle in the radial direction), the average saturation decreased by 43 % compared to the average pore network without a radial gradient.

## 5.4 Concluding Remarks

Numerical and experimental pore networks were employed to design gas diffusion media for directed water transport through the use of pore network modelling and microfluidic fabrication techniques. Randomized pore networks with diagonal and radial biasing show a marked influence on liquid water transport through the two-dimensional media. Unidirectional water transport is achieved through the use of diagonally biased networks. Radial biasing is shown to have the beneficial effect of

decreasing the network saturation, which is a desirable quality in fuel cell GDLs. It was found that with a radial gradient of 1.6 % per obstacle, the average saturation decreased by 43 % compared to the average pore network without a radial gradient. Both the numerical and experimental pore network liquid breakthrough patterns were in good agreement. The results from this chapter indicate that porous media can be designed to have these directed water transport features, and this technique could potentially be applied to design PEMFC GDLs.

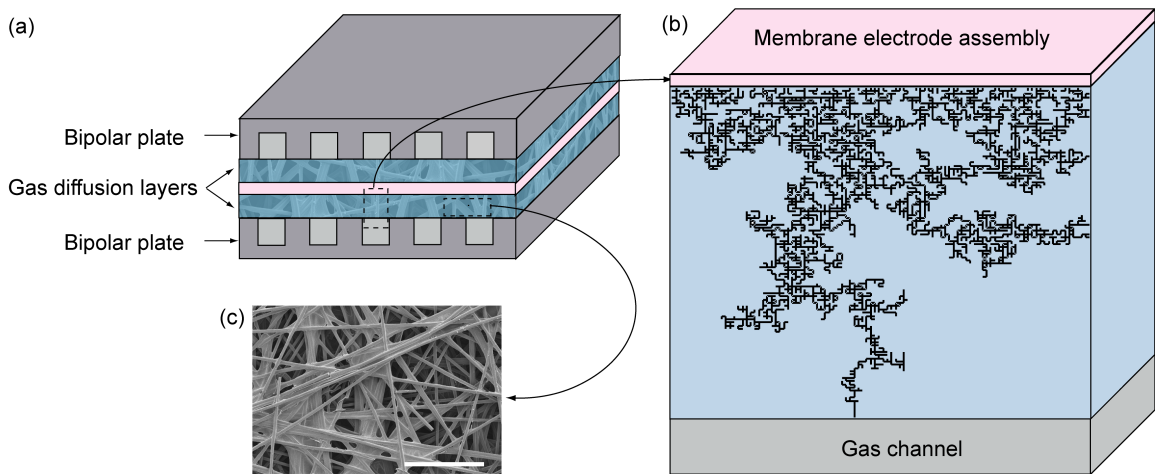


Figure 5.1: Schematic showing pore network modelling results with respect to PEMFC geometry: (a) diagram of a PEMFC, (b) sample numerical pore network breakthrough pattern of a simulated GDL, and (c) SEM image of a Toray TGP-H-060 GDL (length bar represents  $200 \mu\text{m}$ ).

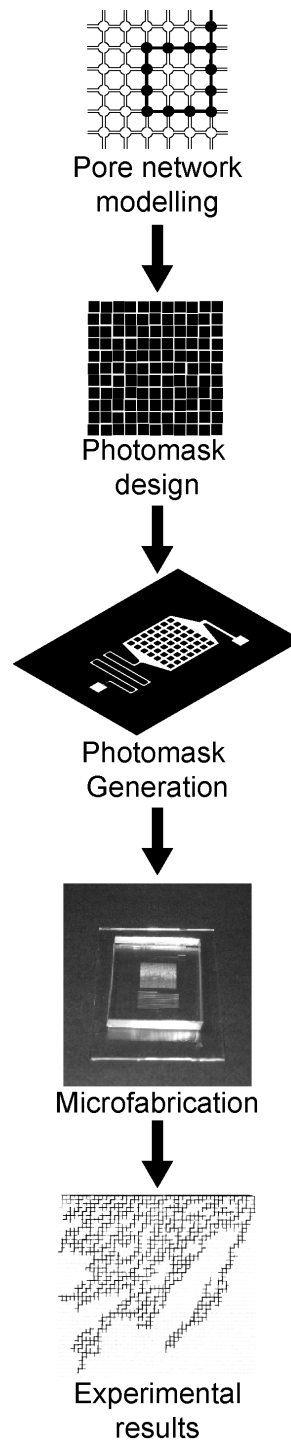


Figure 5.2: Flow diagram illustrating the pore network design and fabrication procedure.

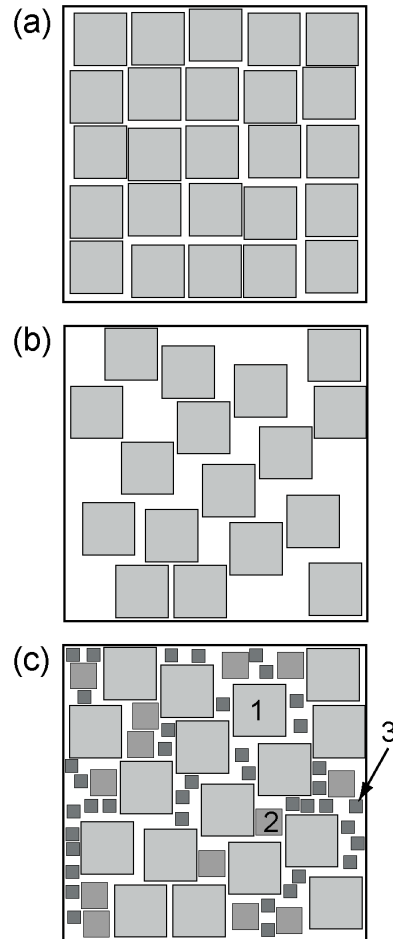


Figure 5.3: Schematic illustrating various methods to construct a microfluidic pore network: (a) randomly perturbing a regular lattice of square obstacles, (b) sequentially placing square obstacles in random locations, and (c) sequentially placing square obstacles of varying sizes in random locations.

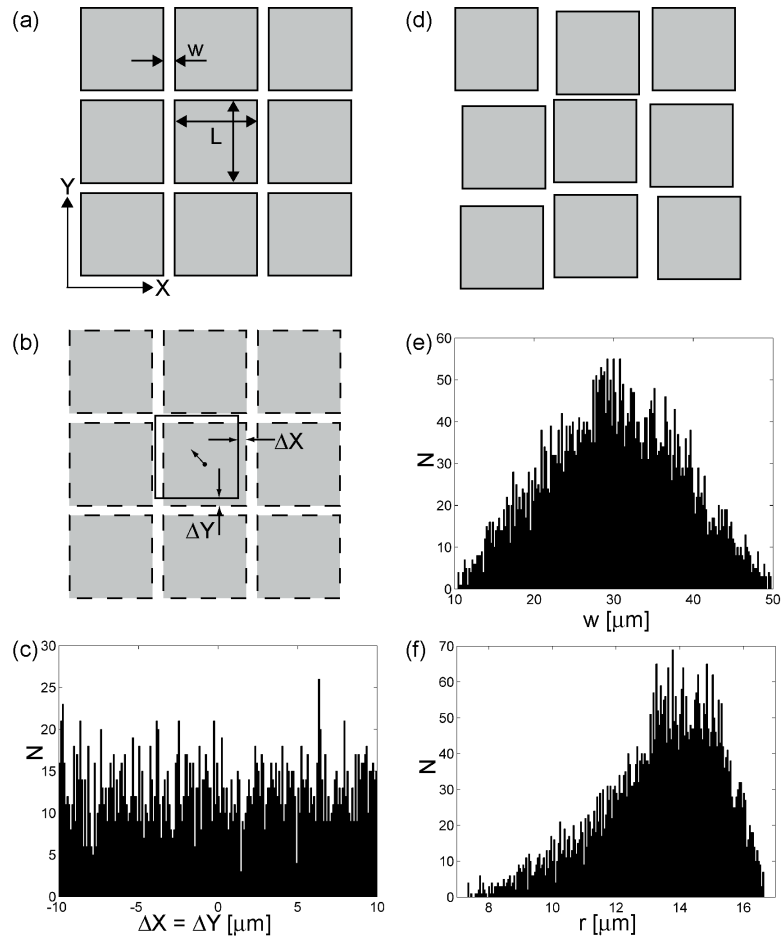


Figure 5.4: Perturbation procedure for generating a photomask: (a) regular square lattice, (b) translation of regular lattice in both the horizontal and vertical directions, (c) uniform distribution of horizontal and vertical translations, (d) resulting arrangement of random pore network, (e) throat width distribution, and (f) hydraulic throat radius distribution.

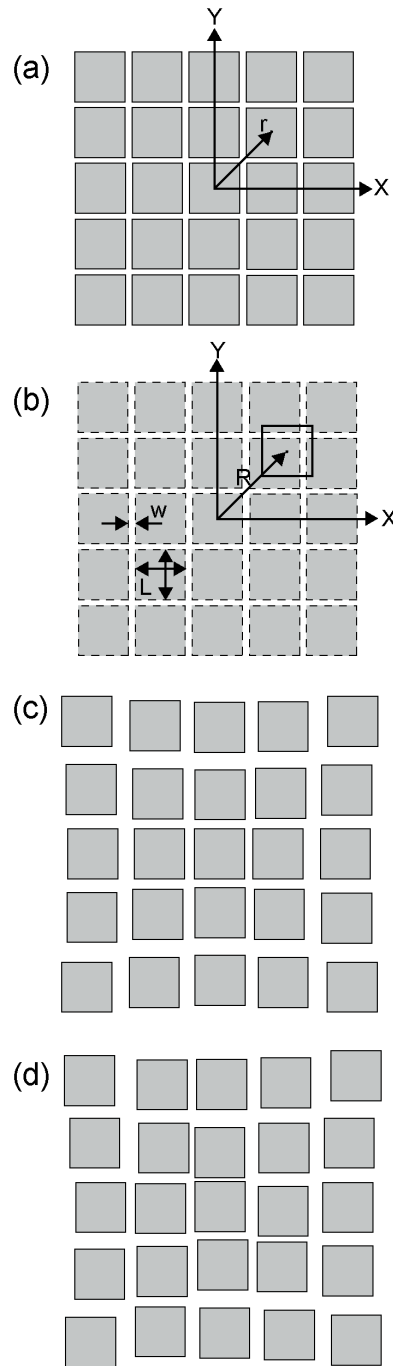


Figure 5.5: Procedure for generating a photomask for a pore network with a prescribed radial gradient: (a) regular square lattice, (b) radial translation of individual square obstacles, (c) network with radial gradient, and (d) random perturbations applied to the network with a radial gradient.

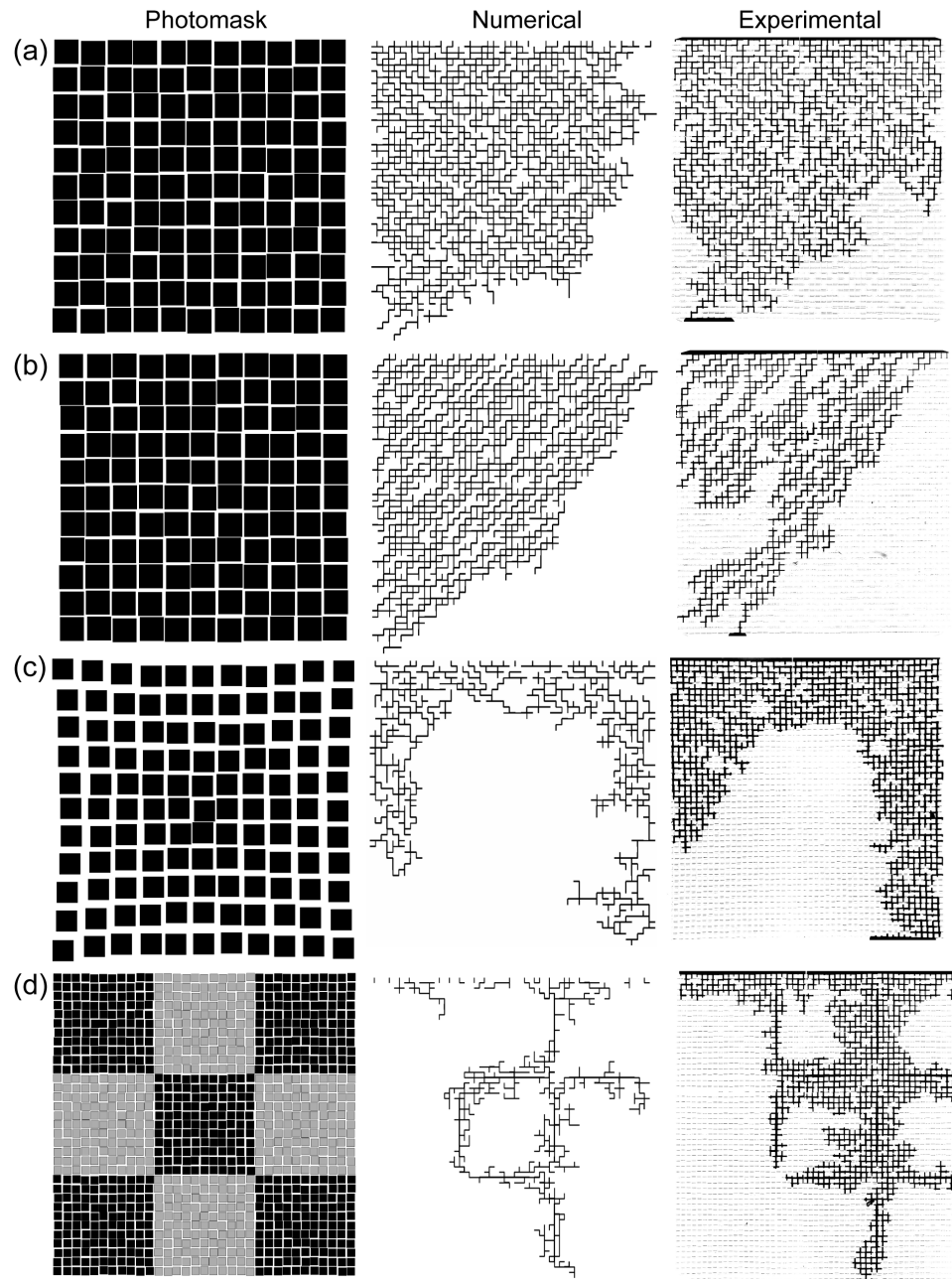


Figure 5.6: Comparison of numerical and experimental random pore network flow patterns at breakthrough: (a) isotropic perturbations, (b) diagonally biased perturbations, (c) radial gradient, and (d) checkerboard pattern with multiple radial gradient patches. Each numerical and experimental result comparison is accompanied by a photomask schematic with a reduced number of obstacles for clarity (along left column).

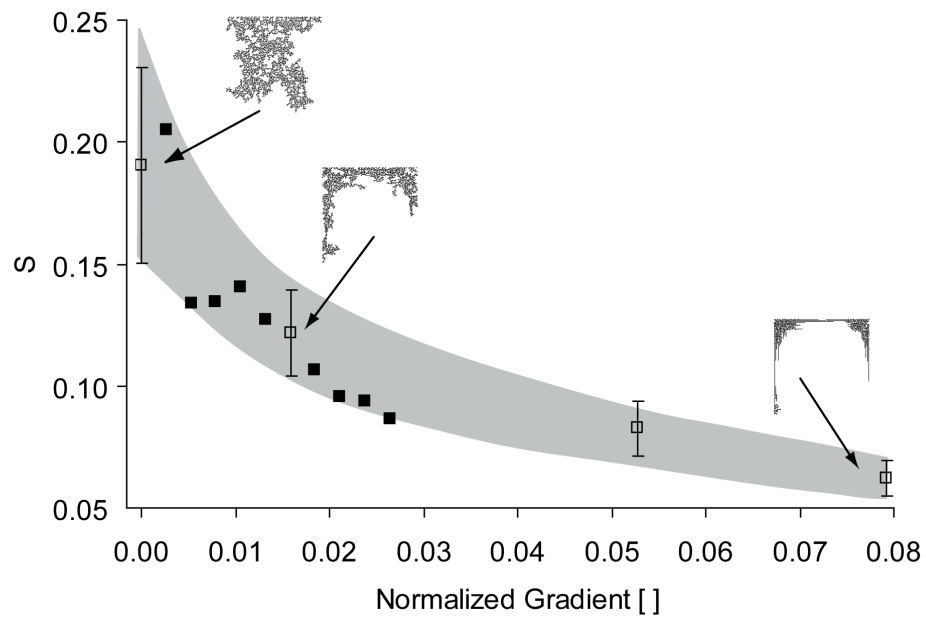


Figure 5.7: Dependence of saturation on increasing radial gradient for a 100 x 100 numerical pore network. The radial gradient is normalized by the average throat width ( $30 \mu\text{m}$ ). Filled squares represent single realizations, where empty squares represent an average value over 100 stochastic realizations with the standard deviation marked with error bars. The shaded region of the plot shows the expected range of saturation values.

## Chapter 6

### Conclusions

Presented in this thesis were three main contributions that provided insight into liquid water transport behaviour in and on the surface of the GDL, as well as insight into how future GDLs could be designed to enhance water management.

In Chapter 3, the effects of compression on liquid water transport in the GDL and the microstructure of the GDL were presented. The experimental apparatus consisted of a GDL clamping device, where liquid water was injected from below the GDL surface. A fluorescein dye solution was employed as a tracer to visualize the evolution of liquid breakthrough. The zones of compression provided preferential locations for water breakthrough, and SEM imaging revealed irreversible damage to the GDL when compressed at typical fuel cell assembly pressures. Furthermore, the severity of GDL damage was proportional to the applied compression pressure. GDL damage consisted of fiber and PTFE breakage, providing localized hydrophilic regions. It was proposed that these localized hydrophilic regions amongst a bulk hydrophobic media provided preferential pathways for liquid water transport.

In Chapter 4, the dynamic behaviour of droplet emergence and detachment in a simulated gas flow channel were investigated and presented. The emergence and detachment of individual droplets were observed with optical microscopy, and it was

found that on an initially dry and hydrophobic GDL, small droplets emerged and detached quickly from the GDL surface. Over time, the water transport regime transitioned into that of slug formation and channel flooding. It was observed that after being exposed to a wet environment, the GDL surface became increasingly prone to droplet pinning, which ultimately hindered droplet detachment and encouraged slug formation. Furthermore, it was observed that the contact line that defined a saturated pore of an emerging droplet in a dry GDL was significantly smaller than that of a GDL that had been exposed to several droplets. Droplets emerging from these larger saturated pores were also larger in size and detached less quickly. Although droplets emerged from preferential breakthrough locations, it was found that these preferential locations changed over time, suggesting that water transport in the GDL consists of a dynamic and interconnected network of water pathways. A supporting CFD VOF simulation illustrated that dominating pathways can recede when a connected pathway becomes dominant.

In Chapter 5, a pore network model featuring invasion percolation with trapping was employed to evaluate the breakthrough pattern predictions of designed porous media. These designed pore networks consisted of randomized porous media with applied diagonal and radial gradients. Experimental microfluidic pores provided validation for the designed networks. Diagonal biasing provided a means of directing water transport in the pore network, while radially biased networks provided the additional feature of reducing the overall network saturation. Since directed water transport and reduced saturation are both beneficial for the PEMFC GDL, it was proposed that biasing of this nature could be applied to improved GDL designs. Specifically, the radial pattern ensures high saturation near the membrane (and thus humidification) while maintaining the majority of the GDL open to the gas phase for efficient reactant transport.

In summary, this thesis presented an analysis of the microscale liquid water transport behaviour in the GDL under the influence of compression and simulated cathode

gas channel conditions. Some characteristics of such flows were identified, including preferential breakthrough locations at compressed regions and tendencies for droplet pinning in a gas channel. These characteristics were accounted for by morphological changes, such as fiber breakage revealing hydrophilic surface areas, and environmental conditioning, such as the build-up of water particles. Furthermore, pore network modeling was presented as a novel technique for designing porous media for directed water transport, with a discussion of why this technique could be applied for designing improved GDLs. Although this work uncovered some interesting characteristics of microscale liquid flows near and on the surface of the GDL, much has yet to be determined before a theoretical framework can be proposed. For instance, due to the opaque nature of the GDL, the microscale flow between the catalyst and top layers of the GDL have yet to be measured.

## 6.1 Future Work

The effect of compression on water transport in the GDL and the GDL microstructure could be extended to other materials, such as other carbon papers and cloth. Investigating the effects of water transport in a cloth GDL with and without compression is of particular interest because cloth GDLs have been shown to provide improved performance over their paper counterparts [4, 32, 136]. Furthermore, the structural properties of carbon cloth vary significantly from that of more rigid carbon paper, and these differences may affect the behaviour of water transport.

In the work presented in this thesis, water transport was observed in the GDL isolated from fuel cell operation. Although these experiments allowed for the isolation and measurement of specific transport phenomena, there are a wide array of variables that can affect realistic transport in an operating fuel cell. For instance, inhomogeneous fuel cell compression [77] could result in various other water transport effects. The associated thermal, gas, and water concentration gradients in fuel cell operation

could also affect transport. Investigation of the microscale transport of liquid water in the top surface layers of the GDL in an operating fuel cell would provide useful feedback for the work conducted in this thesis. A recommended approach to this work is the employment of fluorescence microscopy of a transparent fuel cell. This project could involve the imbibition of fluorescein dye in the catalyst layer or the microporous layer of the MEA. Water produced in the fuel cell would be tagged, and fluorescence microscopy could allow for the through-plane evolution detection at the top surface layers of the fuel cell.

Furthermore, in this thesis, pore network designs were evaluated with a two-dimensional invasion percolation model as well as with two-dimensional hydrophobic microfluidic pore networks. Although it was proposed that this technique for designing porous media for directed water transport could be applied to designing improved GDL materials, there are challenges to consider. First, this approach should be extended to three-dimensional numerical modelling and experimentation. This would provide insight into how this method could be applied in three dimensions, as well as provide an avenue for further design development.

Secondly, conventional GDL materials consist of connected solid fibers, rather than connected void throats in the pore network model. Therefore, the application of a designed pore network to a fibrous GDL requires a careful consideration of how microscale transport in a pore network can be mapped into the microscale transport of a fibrous GDL. Although pore networks are useful for their large scale stochastic modelling of random porous media, it has yet to be determined how accurately smaller scale individual deterministic simulations represent the GDL. Further experimental validations with GDL-like materials could be employed to provide validation for a GDL-representative pore network model.

It should also be kept in mind that GDL materials are generated in either a very structured (woven) or randomized (paper) way, but most importantly, they are generated in very large and continuous quantities that are treated in bulk [131]. Applying

microscale designs to the GDL may be beneficial to increasing the performance of the fuel cell, but at the prohibitive material cost to the fuel cell. Therefore, a consideration of the manufacturability of newly designed GDLs must also be considered.

## References

- [1] S.D. Knights, K.M. Colbow, J. St-Pierre, and D.P. Wilkinson. Aging mechanisms and lifetime of PEFC and DMFC. *Journal of Power Sources*, 127(1-2):127–134, March 2004.
- [2] T. Berning and N. Djilali. A three-dimensional, multi-phase, multicomponent model of the cathode and anode of a PEM fuel cell. *Journal of the Electrochemical Society*, 150(12):A1589–A1598, 2003.
- [3] U. Pasaogullari and C.-Y. Wang. Liquid water transport in gas diffusion layer of polymer electrolyte fuel cells. *Journal of the Electrochemical Society*, 151(3):A399–A406, 2004.
- [4] J.J. Kowal, A. Turhan, K. Heller, J. Brenizer, and M.M. Mench. Liquid water storage, distribution, and removal from diffusion media in PEFCs. *Journal of the Electrochemical Society*, 153(10):A1971–A1978, 2006.
- [5] A. Taniguchi, T. Akita, K. Yasuda, and Y. Miyazaki. Analysis of electrocatalyst degradation in PEMFC caused by cell reversal during fuel starvation. *Journal of Power Sources*, 130:42–49, 2004.
- [6] Q.G. Yan, H. Toghiani, Y.W. Lee, K.W. Liang, and H. Causey. Effect of sub-freezing temperatures on a PEM fuel cell performance, startup and fuel cell components. *Journal of Power Sources*, 160(2):1242–1250, October 2006.

- [7] K. Tüber, D. Pócza, and C. Hebling. Visualization of water buildup in the cathode of a transparent PEM fuel cell. *Journal of Power Sources*, 124:403–414, 2003.
- [8] A. Bazylak, D. Sinton, Z.-S. Liu, and N. Djilali. Effect of compression on liquid water transport and microstructure of PEMFC gas diffusion layers. *Journal of Power Sources*, 163:784–792, 2007.
- [9] A. Bazylak, D. Sinton, and N. Djilali. Dynamic water transport and droplet emergence in PEMFC gas diffusion layers. *Journal of Power Sources*, 176(1):240–246, 2007.
- [10] A. Bazylak, S. Berejnov, B. Markicevic, D. Sinton, and N. Djilali. Numerical and microfluidic pore networks: Towards designs for directed water transport in GDLs. *Electrochimica Acta*, *Accepted March 2008*.
- [11] J. Stumper, M. Löhr, and S. Hamada. Diagnostic tools for liquid water in PEM fuel cells. *Journal of Power Sources*, 143:150–157, 2005.
- [12] S. Tsushima, K. Teranishi, and S. Hirai. Magnetic resonance imaging of the water distribution within a polymer electrolyte membrane in fuel cells. *Electrochemical and Solid State Letters*, 7(9):A269–A272, 2004.
- [13] K.W. Feindel, L.P.-A. LaRocque, D. Starke, S.H. Bergens, and R.E. Wasylshen. In situ observations of water production and distribution in an operating H<sub>2</sub>/O<sub>2</sub> PEM fuel cell assembly using <sup>1</sup>H NMR microscopy. *Journal of the American Chemical Society*, 126:11436–11437, 2004.
- [14] S. Tsushima, K. Teranishi, K. Nishida, and S. Hirai. Water content distribution in a polymer electrolyte membrane for advanced fuel cell system with liquid water supply. *Magnetic Resonance Imaging*, 23:255–258, 2005.

- [15] S. Tsushima, K. Teranishi, and S. Hirai. Water diffusion measurement in fuel-cell SPE membrane by NMR. *Energy*, 30(2-4):235–245, 2005.
- [16] K. Teranishi, S. Tsushima, and S. Hirai. Study of the effect of membrane thickness on the performance of polymer electrolyte fuel cells by water distribution in a membrane. *Electrochemical and Solid State Letters*, 8(6):A281–A284, 2005.
- [17] K. Teranishi, S. Tsushima, and S. Hirai. Analysis of water transport in PEFCs by magnetic resonance imaging measurement. *Journal of the Electrochemical Society*, 153(4):A664–A668, 2006.
- [18] K.R. Minard, V.V. Viswanathan, P.D. Majors, L.Q. Wang, and P.C. Rieke. Magnetic resonance imaging (MRI) of PEM dehydration and gas manifold flooding during continuous fuel cell operation. *Journal of Power Sources*, 161(2):856–863, October 2006.
- [19] K.W. Feindel, S.H. Bergens, and R.E. Wasylishen. Insights into the distribution of water in a self-humidifying H<sub>2</sub>O<sub>2</sub> proton-exchange membrane fuel cell using H NMR microscopy. *Journal of the American Chemical Society*, 128:14192–14199, 2006.
- [20] K.W. Feindel, S.H. Bergens, and R.H. Wasylishen. The use of H NMR microscopy to study proton-exchange membrane fuel cells. *ChemPhysChem*, 7:67–75, 2006.
- [21] K.W. Feindel, S.H. Bergens, and R.E. Wasylishen. The influence of membrane electrode assembly water content on the performance of a polymer electrolyte membrane fuel cell as investigated by H NMR microscopy. *Physical Chemistry Chemical Physics*, 9:1850–1857, 2007.
- [22] K.W. Feindel, S.H. Bergens, and R.E. Wasylishen. Use of hydrogen-deuterium exchange for contrast in <sup>1</sup>H NMR microscopy investigations of an operating PEM fuel cell. *Journal of Power Sources*, 173(1):86–95, November 2007.

- [23] Z. Dunbar and R.I. Masel. Quantitative MRI study of water distribution during operation of a PEM fuel cell using Teflon flow fields. *Journal of Power Sources*, 171(2):678–687, September 2007.
- [24] S. Tsushima, S. Hirai, K. Kitamura, M. Yamashita, and S. Takasel. MRI application for clarifying fuel cell performance with variation of polymer electrolyte membranes: Comparison of water content of a hydrocarbon membrane and a perfluorinated membrane. *Applied Magnetic Resonance*, 32(1-2):233–241, 2007.
- [25] R. Satija, D.L. Jacobson, M. Arif, and S.A. Werner. In situ neutron imaging technique for evaluation of water management systems in operating PEM fuel cells. *Journal of Power Sources*, 129:238–245, 2004.
- [26] D. Kramer, E. Lehmann, G. Frei, P. Vontobel, A. Wokaun, and G.G. Scherer. An on-line study of fuel cell behavior by thermal neutrons. *Nuclear Instruments and Methods in Physics Research A*, 542:52–60, 2005.
- [27] D. Kramer, J. Zhang, R. Shimoi, E. Lehmann, A. Wokaun, K. Shinohara, and G.G. Scherer. In situ diagnostic of two-phase flow phenomena in polymer electrolyte fuel cells by neutron imaging. Part A. Experimental, data treatment, and quantification. *Electrochimica Acta*, 50:2603–2614, 2005.
- [28] N. Pekula, K. Heller, P.A. Chuang, A. Turhan, M.M. Mench, J.S. Brenizer, and K. Unlu. Study of water distribution and transport in a polymer electrolyte fuel cell using neutron imaging. *Nuclear Instruments and Methods in Physics Research A*, 542:134–141, 2005.
- [29] T.A. Trabold, J.P. Owejan, D.L. Jacobson, M. Arif, and P.R. Huffman. In situ investigation of water transport in an operating PEM fuel cell using neutron radiography: Part 1 - Experimental method and serpentine flow field results. *International Journal of Heat and Mass Transfer*, 49 (25-26):4712–4720, 2006.

- [30] J.P. Owejan, T.A. Trabold, D.L. Jacobson, D.R. Baker, D.S. Hussey, and M. Arif. In situ investigation of water transport in an operating PEM fuel cell using neutron radiography: Part 2 - Transient water accumulation in an interdigitated cathode flow field. *International Journal of Heat and Mass Transfer*, 49:4721–4731, 2006.
- [31] A. Turhan, K. Heller, J.S. Brenizer, and M.M. Mench. Quantification of liquid water accumulation and distribution in a polymer electrolyte fuel cell using neutron imaging. *Journal of Power Sources*, 160:1195–1203, 2006.
- [32] J. Zhang, D. Kramer, R. Shimoji, Y. Ono, E. Lehmann, A. Wokaun, K. Shinohara, and G.G. Scherer. In situ diagnostic of two-phase flow phenomena in polymer electrolyte fuel cells by neutron imaging. Part B. Material variations. *Electrochimica Acta*, 51:2715–2727, 2006.
- [33] J.H. Nam and M. Kaviany. Effective diffusivity and water-saturation distribution in single- and two-layer PEMFC diffusion medium. *International Journal of Heat and Mass Transfer*, 46:4595–4611, 2003.
- [34] C. Lim and C.-Y. Wang. Effects of hydrophobic polymer content in GDL in power performance of a PEM fuel cell. *Electrochimica Acta*, 49:4149–4156, 2004.
- [35] P.K. Sinha, P. Halleck, and C.-Y. Wang. Quantification of liquid water saturation in a PEM fuel cell diffusion medium using x-ray microtomography. *Electrochemical and Solid-State Letters*, 9(7):A244–A348, 2006.
- [36] I. Manke, Ch. Hartnig, M. Grünerbel, W. Lehnert, K. Kardjilov, A. Haibel, A. Hilger, J. Banhart, and H. Riesemeier. Investigation of water evolution and transport in fuel cells with high resolution synchrotron x-ray radiography. *Applied Physics Letters*, 90:174105–174105–3, 2007.
- [37] A. Hakenjos, H. Muentert, U. Wittstadt, and C. Hebling. A PEM fuel cell for

- combined measurement of current and temperature distribution, and flow field flooding. *Journal of Power Sources*, 131:213–216, 2004.
- [38] X.G. Yang, F.Y. Zhang, A.L. Lubawy, and C.-Y. Wang. Visualization of liquid water transport in a PEFC. *Electrochemical and Solid-State Letters*, 7(11):A408–A411, 2004.
- [39] J. Borrelli, S.G. Kandlikar, T. Trabold, and J. Owejan. Water transport visualization and two-phase pressure drop measurements in a simulated PEMFC cathode minichannel. *Proceedings of the 3rd International Conference on Microchannels and Minichannels*, pages ICMM2005–75118, June 13-15 2005.
- [40] K. Sugiura, M. Nakata, T. Yodo, Y. Nishiguchi, M. Yamauchi, and Y. Itoh. Evaluation of a cathode gas channel with a water absorption layer/waste channel in a PEFC by using visualization technique. *Journal of Power Sources*, 145:526–533, 2005.
- [41] E.C. Kumbur, K.V. Sharp, and M.M. Mench. Liquid droplet behavior and instability of a polymer electrolyte fuel cell flow channel. *Journal of Power Sources*, 161:333–345, 2006.
- [42] D. Spornjak, S. Advani, and A.K. Prasad. Experimental investigation of liquid water formation and transport in a transparent single-serpentine PEM fuel cell. In *The ASME 4th International Conference on Fuel Cell Science, Engineering and Technology*, FUEL CELL2006-97271, 2006.
- [43] A. Theodorakakos, T. Ous, M. Gavaises, J.M. Nouri, N. Nikolopoulos, and H. Yanagihara. Dynamics of water droplets detached from porous surfaces of relevance to PEM fuel cells. *Journal of Colloid and Interface Science*, 300:673–687, 2006.

- [44] F.-B. Weng, A. Su, C.-Y. Hsu, and C.-Y. Lee. Study of water-flooding behaviour in cathode channel of a transparent proton-exchange membrane fuel cell. *Journal of Power Sources*, 157:674–680, 2006.
- [45] S. Litster, D. Sinton, and N. Djilali. Ex situ visualization of liquid water transport in PEM fuel cell gas diffusion layers. *Journal of Power Sources*, 154:95–105, 2006.
- [46] M.M. Mench, Q.L. Dong, and C.-Y. Wang. In situ water distribution measurements in a polymer electrolyte fuel cell. *Journal of Power Sources*, 124:90–98, 2003.
- [47] M. Watanabe, H. Igarashi, H. Uchida, and F. Hirasawa. Experimental analysis of water behavior in Nafion electrolyte under fuel cell operation. *Journal of Electroanalytical Chemistry*, 399(1-2):239–241, December 1995.
- [48] K. Fushinobu, K. Shimizu, N. Miki, and K. Okazaki. Optical measurement technique of water contents in polymer membrane for PEFCs. *Journal of Fuel Cell Science and Technology*, 3(1):13–17, February 2006.
- [49] J. St-Pierre, A. Wong, J. Diep, and D. Kiel. Demonstration of a residence time distribution method for proton exchange membrane fuel cell evaluation. *Journal of Power Sources*, 164(1):196–202, January 2007.
- [50] J. Diep, D. Kiel, J. St-Pierre, and A. Wong. Development of a residence time distribution method for proton exchange membrane fuel cell evaluation. *Chemical Engineering Science*, 62(3):846–857, February 2007.
- [51] J. St-Pierre. PEMFC in situ liquid-water-content monitoring status. *Journal of the Electrochemical Society*, 154(7):B724–B731, 2007.
- [52] R.J. Bellows, M.Y. Lin, M. Arif, A.K. Thompson, and D. Jacobson. Neutron imaging technique for in situ measurement of water transport gradients within

- nafion in polymer electrolyte fuel cells. *Journal of the Electrochemical Society*, 146(3):1099–1103, March 1999.
- [53] D.J. Ludlow, C.M. Calebrese, S.H. Yu, C.S. Dannehy, D.L. Jacobson, D.S. Hussey, M. Arif, M.K. Jensen, and G.A. Eisman. PEM fuel cell membrane hydration measurement by neutron imaging. *Journal of Power Sources*, 162(1):271–278, November 2006.
- [54] M. A. Hickner, N. P. Siegel, K. S. Chen, D. N. McBrayer, D. S. Hussey, D. L. Jacobson, and M. Arif. Real-time imaging of liquid water in an operating proton exchange membrane fuel cell. *Journal of the Electrochemical Society*, 153(5):A902–A908, 2006.
- [55] J.P. Owejan, T.A. Trabold, J. Gagliardo, D.L. Jacobson, R.N. Carter, D.S. Hussey, and M. Arif. Voltage instability in a simulated fuel cell stack correlated to cathode water accumulation. *Journal of Power Sources*, 171(2):626–633, September 2007.
- [56] Y.S. Chen, H. Peng, D.S. Hussey, D.L. Jacobson, D.T. Tran, T. Abdel-Baset, and M. Biernacki. Water distribution measurement for a PEMFC through neutron radiography. *Journal of Power Sources*, 170(2):376–386, July 2007.
- [57] J.P. Owejan, T.A. Trabold, D.L. Jacobson, M. Arif, and S. G. Kandlikar. Effects of flow field and diffusion layer properties on water accumulation in a PEM fuel cell. *International Journal of Hydrogen Energy*, 32(17):4489–4502, December 2007.
- [58] D.S. Hussey, D.L. Jacobson, M. Arif, J.P. Owejan, J.J. Gagliardo, and T.A. Trabold. Neutron images of the through-plane water distribution of an operating PEM fuel cell. *Journal of Power Sources*, 172:225–228, 2007.

- [59] F. Xu, O. Diat, G. Gebel, and A. Morin. Determination of transverse water concentration profile through MEA in a fuel cell using neutron scattering. *Journal of the Electrochemical Society*, 154(12):B1389–B1398, 2007.
- [60] I. Manke, C. Hartnig, M. Grunerbel, J. Kaczerowski, W. Lehnert, N. Kardjilov, A. Hilger, J. Banhart, W. Treimer, and M. Strobl. Quasi-in situ neutron tomography on polymer electrolyte membrane fuel cell stacks. *Applied Physics Letters*, 90(18):184101, April 2007.
- [61] X.G. Li, I. Sabir, and J. Park. A flow channel design procedure for PEM fuel cells with effective water removal. *Journal of Power Sources*, 163(2):933–942, January 2007.
- [62] H. Ju, G. Luo, and C.-Y. Wang. Probing liquid water saturation in diffusion media of polymer electrolyte fuel cells. *Journal of the Electrochemical Society*, 154(2):B218–B228, 2007.
- [63] D. Spornjak, A.K. Prasad, and S.G. Advani. Experimental investigation of liquid water formation and transport in a transparent single-serpentine PEM fuel cell. *Journal of Power Sources*, 170:334–344, 2007.
- [64] T. Murahashi, H. Kobayashi, and E. Nishiyama. In situ visualization of water droplets in polymer electrolyte fuel cell cathode. *Electrochemistry*, 75(2):261–263, February 2007.
- [65] D.M. Bernardi and M.W. Verbrugge. A mathematical-model of the solid-polymer-electrolyte fuel-cell. *Journal of the Electrochemical Society*, 139(9):2477–2491, September 1992.
- [66] T.E. Springer, M.S. Wilson, and S. Gottesfeld. Modeling and experimental diagnostics in polymer electrolyte fuel-cells. *Journal of the Electrochemical Society*, 140(12):3513–3526, December 1993.

- [67] T.V. Nguyen and R.E. White. A water and heat management model for proton-exchange-membrane fuel-cells. *Journal of the Electrochemical Society*, 140(8):2178–2186, August 1993.
- [68] T. Okada, G. Xie, and Y. Tanabe. Theory of water management at the anode side of polymer electrolyte fuel cell membranes. *Journal of Electroanalytical Chemistry*, 413(1-2):49–65, September 1996.
- [69] K.S. Udell. Heat-transfer in porous-media considering phase-change and capillarity - The heat pipe effect. *International Journal of Heat and Mass Transfer*, 28(2):485–495, 1985.
- [70] W.-K. Lee, C.-H. Ho, J.W. Van Zee, and M. Murthy. The effects of compression and gas diffusion layers on the performance of a PEM fuel cell. *Journal of Power Sources*, 84:45–51, 1999.
- [71] S.-J. Lee, C.-D. Hsu, and C.-H. Huang. Analysis of the fuel cell stack assembly pressure. *Journal of Power Sources*, 145:353–361, 2005.
- [72] J. Ge, A. Higier, and H. Liu. Effect of gas diffusion layer compression on PEM fuel cell performance. *Journal of Power Sources*, 159:922–927, 2006.
- [73] T. Ous and C. Arcoumanis. Effect of compressive force on the performance of a proton exchange membrane fuel cell. *Proceedings of the Institution of Mechanical Engineers Part C - Journal of Mechanical Engineering Science*, 221(9):1067–1074, September 2007.
- [74] J. Itonen, M. Mikkola, and G. Lindbergh. Flooding of gas diffusion backing in PEFCs - Physical and electrochemical characterization. *Journal of the Electrochemical Society*, 151(8):A1152–A1161, 2004.
- [75] S. Escribano, J.-F. Blachot, J. Ethève, A. Morin, and R. Mosdale. Character-

- ization of PEMFCs gas diffusion layers properties. *Journal of Power Sources*, 156:8–13, 2006.
- [76] T. Matsuura, M. Kato, and M. Hori. Study on metallic bipolar plate for proton exchange membrane fuel cell. *Journal of Power Sources*, 161(1):74–78, October 2006.
- [77] I. Nitta, T. Hottinen, O. Himanen, and M. Mikkola. Inhomogeneous compression of PEMFC gas diffusion layer Part I. Experimental. *Journal of Power Sources*, 171(1):26–36, September 2007.
- [78] P. Zhou and C.W. Wu. Numerical study on the compression effect of gas diffusion layer on PEMFC performance. *Journal of Power Sources*, 170(1):93–100, June 2007.
- [79] T. Hottinen, O. Himanen, S. Karvonen, and I. Nitta. Inhomogeneous compression of PEMFC gas diffusion layer Part II. Modeling the effect. *Journal of Power Sources*, 171(1):113–121, September 2007.
- [80] T. Hottinen and O. Himanen. PEMFC temperature distribution caused by inhomogeneous compression of GDL. *Electrochemistry Communications*, 9(5):1047–1052, May 2007.
- [81] E.C. Kumbur, K.V. Sharp, and M.M. Mench. Validated leverett approach for multiphase flow in PEFC diffusion media. II. Compression effect. *Journal of the Electrochemical Society*, 154 (12):B1305–B1314, 2007.
- [82] P.M. Wilde, M. Mändle, M.b Murata, and N. Berg. Structural and physical properties of GDL and GDL/BPP combinations and their influence on PEMFC performance. *Fuel Cells*, 4 (3):180–184, 2004.
- [83] I. Fatt. The network model of porous media I. Capillary pressure characteristics.

- Petroleum Transactions, the American Institute of Mining, Metallurgical, and Petroleum Engineers (AIME)*, 207:144–159, 1956.
- [84] I. Fatt. The network model of porous media II. Dynamic properties of a single size tube network. *Petroleum Transactions, the American Institute of Mining, Metallurgical, and Petroleum Engineers (AIME)*, 207:160–163, 1956.
- [85] I. Fatt. The network model of porous media III. Dynamic properties of networks with tube radius distribution. *Petroleum Transactions, the American Institute of Mining, Metallurgical, and Petroleum Engineers (AIME)*, 207:164–181, 1956.
- [86] S.R. Broadbent and J.M. Hammersley. Percolation processes I. Crystals and mazes. *Proceedings of the Cambridge Philosophical Society*, 53:629–641, 1957.
- [87] P.M. Adler. Multiphase flow in porous media. *Annual Review of Fluid Mechanics*, 20:35–59, 1988.
- [88] S. Levine, P. Reed, G. Shutts, and G. Neale. Some aspects of wetting-dewetting of a porous-medium. *Powder Technology*, 17(2):163–181, 1977.
- [89] R.G. Larson, L.E. Scriven, and H.T. Davis. Percolation theory of residual phases in porous-media. *Nature*, 268(5619):409–413, 1977.
- [90] P.G. DeGennes and E. Guyon. General laws for injection of a fluid in a porous-medium. *Journal de Mecanique*, 17(3):403–432, 1978.
- [91] D. Stauffer and A. Aharony. *Introduction to percolation theory*. Taylor & Francis, 1992.
- [92] J.M. Hammersley. Percolation processes: Lower bounds for the critical probability. *The Annals of Mathematical Statistics*, 28(3):790–795, 1957.
- [93] R. Chandler, J. Koplik, K. Lerman, and J.F. Willemsen. Capillary displacement and percolation in porous media. *Journal of Fluid Mechanics*, 119:249–267, 1982.

- [94] C. Lin and M.H. Cohen. Quantitative methods for microgeometric modelling. *Journal of Applied Physics*, 56(6):4152–4165, 1982.
- [95] D. Wilkinson and J.F. Willemsen. Invasion percolation: a new form of percolation theory. *Journal of Physics A: Mathematical and General*, 16:3365–3376, 1983.
- [96] A.C. Payatakes. Dynamics of oil ganglia during immiscible displacement in water-wet porous media. *Annual Review of Fluid Mechanics*, 14:365–393, 1982.
- [97] J. Koplik and T.J. Lasseeter. Two-phase flow in random network models of porous media. *Society of Petroleum Engineers Journal*, 25 (1):89–100, 1985.
- [98] A. B. Dixit, S.R. McDougall, K.S. Sorbie, and J.S. Buckley. Pore-scale modeling of wettability effects and their influence on oil recovery. *SPE Reservoir Evaluation and Engineering*, 2(1):25–36, 1999.
- [99] M.S. Valavanides and A.C. Payatakes. True-to-mechanism model of steady-state two-phase flow in porous media, using decomposition into prototype flows. *Advances in Water Resources*, 24:385–407, 2001.
- [100] L. Paterson. Trapping thresholds in invasion percolation. *Physical Review E*, 66:1–6, 2002.
- [101] M.G. Bernadiner. A capillary microstructure of the wetting front. *Transport in porous media*, 30:251–265, 1998.
- [102] K.E. Thompson. Pore-scale modeling of fluid transport in disordered fibrous materials. *American Institute of Chemical Engineers Journal*, 48 (7):1369–1389, 2002.
- [103] M.J. Blunt. Flow in porous media - pore-network models and multiphase flow. *Current Opinion in Colloid & Interface Science*, 6:197–207, 2001.

- [104] R. Lenormand and C. Zarcone. Invasion percolation in an etched network: measurement of a fractal dimension. *Physical Review Letters*, 54 (20):2226–2229, 1985.
- [105] R. Lenormand, E. Touboul, and C. Zarcone. Numerical models and experiments on immiscible displacements in porous media. *Journal of Fluid Mechanics*, 189:165–187, 1988.
- [106] R. Lenormand and C. Zarcone. Capillary fingering: percolation and fractal dimension. *Transport in Porous Media*, 4:599–612, 1989.
- [107] A. Birovljev, L. Furuberg, F. Feder, T. Jossang, A. Maloy, and A. Aharony. Gravity invasion percolation in two dimensions. *Physical Review Letters*, 67(5):584–587, 1991.
- [108] O. Vizika, D.G. Avraam, and A.C. Payatakes. On the role of the viscosity ratio during low-capillary-number forced imbibition in porous media. *Journal of Colloid and Interface Science*, 165:386–401, 1994.
- [109] B. Xu and Y.C. Yortsos. Invasion percolation with viscous forces. *Physical Review E*, 57 (1):739–751, 1998.
- [110] C.D. Tsakiroglou, M. Theodoropoulou, V. Karoutsos, D. Papanicolaou, and V. Sygouni. Experimental study of the immiscible displacement of shear-thinning fluids in pore networks. *Journal of Colloid Interface Science*, 267:217–232, 2003.
- [111] E. Kossel, M. Weber, and R. Kimmich. Visualization of transport: NMR microscopy experiments with model objects for porous media with pore sizes down to 50 $\mu\text{m}$ . *Solid State Nuclear Magnetic Resonance*, 25:28–34, 2004.
- [112] C. Perrin, P.M.J. Tardy, K.S. Sorbie, and J.C. Crawshaw. Experimental and

- modeling study of newtonian and non-newtonian fluid flow in pore network micromodels. *Journal of Colloid and Interface Science*, 295:542–550, 2006.
- [113] M.I.J. van Dijke, K.S. Sorbie, and A. Danesh. Three-phase flow WAG processes in mixed-wet porous media: pore-scale network simulations and comparison with water-wet micromodel experiments. *SPE Journal*, 9(1):57–66, 2004.
- [114] M.I.J. van Dijke, K.S. Sorbie, M. Sohrabi, and A. Danesh. Simulation of WAG floods in an oil-wet micromodel using a 2-D pore-scale network model. *Journal of Petroleum Science and Engineering*, 52:71–86, 2006.
- [115] Viatcheslav Berejnov, Ned Djilali, and David Sinton. Lab-on-chip methodologies for the study of transport in porous media: energy applications. *Lab Chip*, 8:1–5, 2008.
- [116] R. Lenormand and C. Zarcone. Role of roughness and edges during imbibition in square capillaries. *Proceedings of the 59th Annual Technical Conference and Exhibition of SPE AIME, Houston, Texas*, page SPE 13264, 1984.
- [117] U. Oxaal, M. Murat, F. Bojer, A. Aharony, J. Feder, and T. Jossang. Viscous fingering on percolation cluster. *Nature*, 329:32–37, 1987.
- [118] M.A. Theodoropoulou, V. Sygouni, V. Karoutsos, and C.D. Tsakiroglou. Relative permeability and capillary pressure functions of porous media as related to the displacement growth pattern. *International Journal of Multiphase Flow*, 31:1155–1180, 2005.
- [119] M. Sahimi. Flow phenomena in rocks: from continuum models to fractals, percolation, cellular automata, and simulated annealing. *Reviews of Modern Physics*, 65 (4):1393–1534, 1993.
- [120] G.N. Constantinides and A.C. Payatakes. Network simulation of steady-state

- two-phase flow in consolidated porous media. *American Institute of Chemical Engineers Journal*, 42 (2):369–382, 1996.
- [121] J.T. Gostick, M.A. Ioannidis, M.W. Fowler, and M.D. Pritzker. Pore network modeling of fibrous gas diffusion layers for polymer electrolyte membrane fuel cells. *Journal of Power Sources*, 173 (1):277–290, 2007.
- [122] B. Markicevic, A. Bazylak, and N. Djilali. Determination of transport parameters for multiphase flow in porous gas diffusion electrodes using a capillary network model. *Journal of Power Sources*, 171(2):706–717, 2007.
- [123] P.K. Sinha and C.-Y. Wang. Pore-network modeling of liquid water transport in gas diffusion layer of a polymer electrolyte fuel cell. *Electrochimica Acta*, 52:7936–7945, 2007.
- [124] K. Jiao and B. Zhou. Innovative gas diffusion layers and their water removal characteristics in PEM fuel cell cathode. *Journal of Power Sources*, 169:296–314, 2007.
- [125] A.Z. Weber and R.M. Darling. Understanding porous water-transport plates in polymer-electrolyte fuel cells. *Journal of Power Sources*, 168:191–199, 2007.
- [126] C.R. Buie, J.D. Posner, T. Fabian, S.-W. Cha, D. Kim, F.B. Prinz, J.K. Eaton, and J.G. Santiago. Water management in proton exchange membrane fuel cells using integrated electroosmotic pumping. *Journal of Power Sources*, 161:191–202, 2006.
- [127] S. Litster, C.R. Buie, T. Fabian, J.K. Eaton, and J.G. Santiago. Active water management for PEM fuel cells. *Journal of the Electrochemical Society*, 154 (10):B1049–B1058, 2007.
- [128] S. Litster and N. Djilali. *Transport Phenomena in Fuel Cells*, chapter Two-

- Phase Transport in Porous Gas Diffusion Electrodes, pages 175–213. WIT Press, Southampton UK, 2005. Editors: Faghri, M. AND Sundén, B.
- [129] D. Sinton. Microscale flow visualization. *Microfluid Nanofluid*, 1:2–21, 2004.
- [130] H. Anderson, S. Fu, T.G. Myers, and C.P. Thompson. UV induced fluorescence and comparative velocity measurement of thin liquid films. *Proceedings of the 9th International Symposium On Flow Visualization*, pages (Paper 8) 1–7, 2000.
- [131] M. Mathias, J. Roth, J. Fleming, and W. Lehnert. *Handbook of Fuel Cells*, chapter Diffusion media materials and characterization, pages 1–21. John Wiley & Sons, Ltd., New York, 2003.
- [132] V.P. Schulz, J. Becker, A. Wiegmann, P.P. Mukherjee, and C.-Y. Wang. Modeling of two-phase behaviour in the gas diffusion medium of PEMFCs via full morphology approach. *Journal of the Electrochemical Society*, 154(4):B419–B426, 2007.
- [133] C. W. Hirt and B.D. Nichols. Volume of fluid (VOF) method for the dynamics of free boundaries. *Journal of Computational Physics*, 39(1):201–225, 1981.
- [134] X. Zhu, P.C. Sui, and N. Djilali. Numerical simulation of emergence of a water droplet from a pore into a microchannel gas stream. *Microfluidics & Nanofluidics*, In Print, 2007.
- [135] Microchem. Microchem NANO SU-8: Negative tone photoresist formulations 50-100.
- [136] Y. Wang, C.-Y. Wang, and K.S. Chen. Elucidating differences between carbon paper and carbon cloth in polymer electrolyte fuel cells. *Electrochimica Acta*, 52:3965–3975, 2007.